



The TESS-Keck Survey. XI. Mass Measurements for Four Transiting Sub-Neptunes Orbiting K Dwarf TOI-1246

Downloaded from: <https://research.chalmers.se>, 2025-12-05 03:27 UTC

Citation for the original published paper (version of record):

Turtelboom, Weiss, L., Dressing, C. et al (2022). The TESS-Keck Survey. XI. Mass Measurements for Four Transiting Sub-Neptunes Orbiting K Dwarf TOI-1246. *Astronomical Journal*, 163(6). <http://dx.doi.org/10.3847/1538-3881/ac69e5>

N.B. When citing this work, cite the original published paper.



The TESS-Keck Survey. XI. Mass Measurements for Four Transiting Sub-Neptunes Orbiting K Dwarf TOI-1246

Emma V. Turtelboom¹ , Lauren M. Weiss² , Courtney D. Dressing¹ , Grzegorz Nowak^{3,4} , Enric Pallé^{3,4} , Corey Beard⁵ , Sarah Blunt⁶ , Casey Brinkman⁷ , Ashley Chontos^{7,49} , Zachary R. Clayton⁷ , Fei Dai⁸ , Paul A. Dalba^{9,10,50} , Steven Giacalone¹ , Erica Gonzales⁹ , Caleb K. Harada^{1,49} , Michelle L. Hill¹⁰ , Rae Holcomb⁵ , Judith Korth¹¹ , Jack Lubin⁵ , Thomas Masseron^{3,4} , Mason MacDougall¹² , Andrew W. Mayo^{1,13} , Teo Močnik¹⁴ , Joseph M. Akana Murphy^{9,49} , Alex S. Polanski¹⁵ , Malena Rice^{16,49} , Ryan A. Rubenzahl^{6,49} , Nicholas Scarsdale⁹ , Keivan G. Stassun¹⁷ , Dakotah B. Tyler¹² , Judah Van Zandt¹⁸ , Ian J. M. Crossfield¹⁵ , Hans J. Deeg^{3,4} , Benjamin Fulton¹⁹ , Davide Gandolfi²⁰ , Andrew W. Howard⁶ , Dan Huber⁷ , Howard Isaacson^{1,21} , Stephen R. Kane¹⁰ , Kristine W. F. Lam²² , Rafael Luque²³ , Eduardo L. Martín^{3,4,24} , Giuseppe Morello^{4,25} , Jaume Orell-Miquel^{4,25} , Erik A. Petigura¹⁸ , Paul Robertson⁵ , Arpita Roy^{26,27} , Vincent Van Eylen²⁸ , David Baker²⁹ , Alexander A. Belinski³⁰ , Allyson Bieryla³¹ , David R. Ciardi³² , Karen A. Collins³¹ , Neil Cutting²⁹ , Devin J. Della-Rose³³ , Taylor B. Ellingsen³⁴ , E. Furlan³² , Tianjun Gan³⁵ , Crystal L. Gnilka^{32,36} , Pere Guerra³⁷ , Steve B. Howell³⁶ , Mary Jimenez³⁴ , David W. Latham³¹ , Maude Larivière^{38,39} , Kathryn V. Lester³⁶ , Jorge Lillo-Box⁴⁰ , Lindy Luker²⁹ , Christopher R. Mann^{39,41} , Peter P. Plavchan⁴² , Boris Safonov³⁰ , Brett Skinner²⁹ , Ivan A. Strakhov³⁰ , Justin M. Wittrock⁴² , Douglas A. Caldwell⁴³ , Zahra Essack^{44,45} , Jon M. Jenkins³⁶ , Elisa V. Quintana⁴⁶ , George R. Ricker⁴⁵ , Roland Vanderspek⁴⁵ , S. Seager^{44,45,47} , and Joshua N. Winn⁴⁸

¹ Department of Astronomy, 501 Campbell Hall, University of California, Berkeley, CA 94720, USA; eturtelboom@berkeley.edu

² Department of Physics, University of Notre Dame, Notre Dame, IN, 46556, USA

³ Instituto de Astrofísica de Canarias (IAC), E-38200 La Laguna, Tenerife, Spain

⁴ Departamento de Astrofísica, Universidad de La Laguna (ULL), E-38206 La Laguna, Tenerife, Spain

⁵ Department of Physics & Astronomy, University of California Irvine, Irvine, CA 92697, USA

⁶ Department of Astronomy, California Institute of Technology, Pasadena, CA 91125, USA

⁷ Institute for Astronomy, University of Hawai'i, 2680 Woodlawn Drive, Honolulu, HI 96822, USA

⁸ Division of Geological and Planetary Sciences, 1200 E California Boulevard, Pasadena, CA, 91125, USA

⁹ Department of Astronomy and Astrophysics, University of California, Santa Cruz, CA 95064, USA

¹⁰ Department of Earth and Planetary Sciences, University of California Riverside, 900 University Avenue, Riverside, CA 92521, USA

¹¹ Department of Space, Earth and Environment, Astronomy and Plasma Physics, Chalmers University of Technology, SE-412 96 Gothenburg, Sweden

¹² Astronomy Department, 475 Portola Plaza, University of California, Los Angeles, CA 90095, USA

¹³ Centre for Star and Planet Formation, Natural History Museum of Denmark & Niels Bohr Institute, University of Copenhagen, Øster Voldgade 5-7, DK-1350 Copenhagen K., Denmark

¹⁴ Gemini Observatory/NSF's NOIRLab, 670 N. A'ohoku Place, Hilo, HI 96720, USA

¹⁵ Department of Physics and Astronomy, University of Kansas, Lawrence, KS, USA

¹⁶ Department of Astronomy, Yale University, New Haven, CT 06511, USA

¹⁷ Department of Physics and Astronomy, Vanderbilt University, Nashville, TN 37235, USA

¹⁸ Department of Physics & Astronomy, University of California Los Angeles, Los Angeles, CA 90095, USA

¹⁹ NASA Exoplanet Science Institute/Caltech-IPAC, MC 314-6, 1200 E California Boulevard, Pasadena, CA 91125, USA

²⁰ Dipartimento di Fisica, Università degli Studi di Torino, I-10125, Torino, Italy

²¹ Centre for Astrophysics, University of Southern Queensland, Toowoomba, QLD, Australia

²² German Aerospace Center, Institute of Planetary Research, D-12489 Berlin, Germany

²³ Instituto de Astrofísica de Andalucía (IAA-CSIC), Glorieta de la Astronomía s/n, E-18008 Granada, Spain

²⁴ Consejo Superior de Investigaciones Científicas (CSIC), E-28006 Madrid, Spain

²⁵ Instituto de Astrofísica de Canarias (IAC), E-38205 La Laguna, Tenerife, Spain

²⁶ Space Telescope Science Institute, 3700 San Martin Drive, Baltimore, MD 21218, USA

²⁷ Department of Physics and Astronomy, Johns Hopkins University, 3400 N Charles Street, Baltimore, MD 21218, USA

²⁸ Mullard Space Science Laboratory, University College London, Holmbury St Mary, Dorking, Surrey RH5 6NT, UK

²⁹ Physics Department, Austin College, Sherman, TX 75090, USA

³⁰ Sternberg Astronomical Institute, M.V. Lomonosov Moscow State University, 13, Universitetskij pr., 119234, Moscow, Russia

³¹ Center for Astrophysics | Harvard & Smithsonian, 60 Garden Street, Cambridge, MA 02138, USA

³² NASA Exoplanet Science Institute, Caltech/IPAC, Mail Code 100-22, 1200 E. California Boulevard, Pasadena, CA 91125, USA

³³ Physics and Meteorology Department, 2354 Fairchild Drive, Suite 2A91, U.S. Air Force Academy, CO 80840, USA

³⁴ Department of Physics and Astronomy, George Mason University, 4400 University Drive MSN 3F3, Fairfax, VA 22030, USA

³⁵ Department of Astronomy, Tsinghua University, Beijing 100084, People's Republic of China

³⁶ NASA Ames Research Center, Moffett Field, CA 94035, USA

³⁷ Observatori Astronòmic Albanyà, Camí de Bassegoda S/N, Albanyà E-17733, Girona, Spain

³⁸ Department of Physics, 3600 rue University, McGill University, Montréal, Québec, H3A 2T8, Canada

³⁹ Institute for Research on Exoplanets (iREx), Université de Montréal, Canada

⁴⁰ Centro de Astrobiología (CAB, CSIC-INTA), Depto. de Astrofísica, ESAC campus, E-28692, Villanueva de la Cañada (Madrid), Spain

⁴¹ Université de Montréal, Montréal, QC H2V 0B3, Canada

⁴² Department of Physics and Astronomy, George Mason University, 4400 University Drive, Fairfax, VA 22030, USA

⁴³ SETI Institute, Mountain View, CA 94043, USA

⁴⁴ Department of Earth, Atmospheric and Planetary Sciences, MIT, Cambridge, MA 02139, USA

⁴⁵ Department of Physics and Kavli Institute for Astrophysics and Space Research, MIT, Cambridge, MA 02139, USA

⁴⁶ NASA Goddard Space Flight Center, Greenbelt, MD 20771, USA

⁴⁷ Department of Aeronautics and Astronautics, MIT, 77 Massachusetts Avenue, Cambridge, MA 02139, USA

⁴⁸ Department of Astrophysical Sciences, Princeton University, Princeton, NJ 08544, USA
 Received 2021 December 23; revised 2022 April 7; accepted 2022 April 22; published 2022 May 25

Abstract

Multiplanet systems are valuable arenas for investigating exoplanet architectures and comparing planetary siblings. TOI-1246 is one such system, with a moderately bright K dwarf ($V = 11.6$, $K = 9.9$) and four transiting sub-Neptunes identified by TESS with orbital periods of 4.31, 5.90, 18.66, and 37.92 days. We collected 130 radial velocity observations with Keck/HIRES and TNG/HARPS-N to measure planet masses. We refit the 14 sectors of TESS photometry to refine planet radii ($2.97 \pm 0.06 R_{\oplus}$, $2.47 \pm 0.08 R_{\oplus}$, $3.46 \pm 0.09 R_{\oplus}$, and $3.72 \pm 0.16 R_{\oplus}$) and confirm the four planets. We find that TOI-1246 e is substantially more massive than the three inner planets ($8.1 \pm 1.1 M_{\oplus}$, $8.8 \pm 1.2 M_{\oplus}$, $5.3 \pm 1.7 M_{\oplus}$, and $14.8 \pm 2.3 M_{\oplus}$). The two outer planets, TOI-1246 d and TOI-1246 e, lie near to the 2:1 resonance ($P_e/P_d = 2.03$) and exhibit transit-timing variations. TOI-1246 is one of the brightest four-planet systems, making it amenable for continued observations. It is one of only five systems with measured masses and radii for all four transiting planets. The planet densities range from 0.70 ± 0.24 to $3.21 \pm 0.44 \text{ g cm}^{-3}$, implying a range of bulk and atmospheric compositions. We also report a fifth planet candidate found in the RV data with a minimum mass of $25.6 \pm 3.6 M_{\oplus}$. This planet candidate is exterior to TOI-1246 e, with a candidate period of 93.8 days, and we discuss the implications if it is confirmed to be planetary in nature.

Unified Astronomy Thesaurus concepts: Exoplanet astronomy (486); Mini Neptunes (1063); Exoplanets (498); Radial velocity (1332); Transits (1711); Transit photometry (1709); Transit timing variation method (1710); Exoplanet systems (484)

1. Introduction

While we have known for centuries that our own Solar System hosts multiple planets, it was only in the late twentieth century that we confirmed the existence of multiple planets around other stars. In fact, the first exoplanets ever discovered were two planets orbiting the pulsar PSR 1257 + 12 (Wolszczan & Frail 1992), i.e., the first known exoplanetary system was also the first known multiplanet system. In the years after this finding, ground-based radial velocity (RV) surveys found additional planets orbiting known planet hosts (Butler et al. 1999; Fischer et al. 2002), and methods were developed to appropriately model multiplanet RV signals (Wright & Howard 2009). Still later, the prevalence of multiplanet systems was brought to light by large surveys of transiting planets such as the Kepler and TESS missions. Of the 2385 confirmed planets discovered using the transit method by the Kepler mission, 1156 were found to be in 458 multiplanet systems.⁵¹ The TESS mission is continuing to expand our understanding of exoplanets by searching for bright, nearby stars that host transiting planets. About 15% of TESS Objects of Interest (TOIs) are predicted to be in systems with multiple transiting planets (Huang et al. 2018). While 34 TESS systems host multiple confirmed planets, only four systems host four or more transiting planets: HD 108236 (Bonfanti et al. 2021), L98-59 (Demangeon et al. 2021), TOI-178 (Leleu et al. 2021), and TOI-561 (Lacedelli et al. 2021; Weiss et al. 2021). In this work, we add to this growing—but currently small—sample.

This paper is the eleventh (TKS-XI) in a series of papers by the TESS-Keck Survey (TKS). TKS is a collaboration spanning several institutions that pools time on the Keck I

telescope on Maunakea. Using the High Resolution Echelle Spectrograph (HIRES; Vogt et al. 1994), TKS conducts spectroscopy of TOIs in order to determine planet masses and host star properties for a variety of science goals. TKS-0 (Chontos et al. 2021) is a more comprehensive description of the TKS program science goals and target selection.

The TOI-1246 system hosts four transiting sub-Neptune-sized planets orbiting a K dwarf: TOI-1246 b (formerly TOI-1246.02), TOI-1246c (formerly TOI-1246.03), TOI-1246 d (formerly TOI-1246.01), and TOI-1246 e (formerly TOI-1246.04). The four transiting planets lie within 0.5 au of the host star ($P_b = 4.31$ days, $P_c = 5.90$ days, $P_d = 18.66$ days, and $P_e = 37.92$ days). The inner three planets are smaller than the outermost transiting planet ($R_b = 2.97 \pm 0.06 R_{\oplus}$, $R_c = 2.47 \pm 0.08 R_{\oplus}$, $R_d = 3.46 \pm 0.09 R_{\oplus}$, and $R_e = 3.72 \pm 0.16 R_{\oplus}$). By studying multiple planets orbiting a single host star, we can study planets with a shared formation and evolutionary history.

TOI-1246 was observed as part of the TKS subprogram to obtain follow-up observations and determine masses for planets in multiplanet systems observed by TESS. This paper also includes RV data collected using TNG/HARPS-N. The paper is structured as follows. In Section 2, we describe the TESS photometry, as well as the follow-up spectroscopic, photometric, and imaging observations used in our analysis of the TOI-1246 system. In Section 3, we characterize the host star and investigate stellar rotation and activity. In Section 4, we refit the TESS photometry to refine transit parameters, and analyze the two RV data sets in order to determine planet masses and constrain planetary orbits. We also measure transit-timing variations (TTVs) and investigate system stability. Finally, in Section 5, we discuss the planet masses and densities in the context of other multiplanet systems, as well as the suitability of this system for further studies involving atmospheric characterization. We also discuss the system architecture and the possible explanations and implications of the fifth planet candidate in Section 5, and we conclude this work in Section 6.

⁴⁹ NSF Graduate Research Fellow.

⁵⁰ NSF Astronomy and Astrophysics Postdoctoral Fellow.

⁵¹ NASA Exoplanet Archive (NASA Exoplanet Science Institute 2020), exoplanetarchive.ipac.caltech.edu, accessed on 2021 November 8.



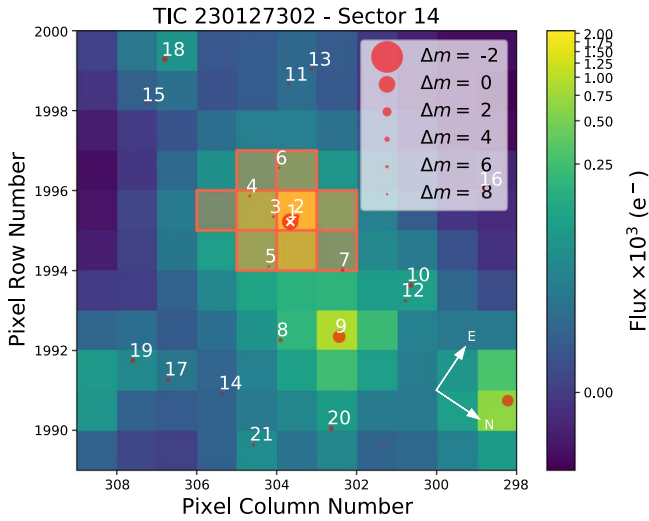


Figure 1. Sector 14 TESS Target Pixel File for TOI-1246 with the SPOC pipeline aperture overlaid in red. TOI-1246 is indicated with a white cross and labeled as target 1. The Gaia DR2 sources in the field are shown by red dots, scaled in size to the difference in magnitude with TOI-1246. The TESS pixel scale is $21 \text{ arcsec/pixel}^{-1}$.

2. Observations

In this section, we describe the three types of observations of TOI-1246: photometric data (from the TESS mission and seeing-limited photometry collected by the TESS SG1 Working Group), spectroscopic data (reconnaissance and precision spectra), and high-resolution imaging data (speckle, lucky, and AO). Additional figures describing the observations discussed here can be found on ExoFOP-TESS.⁵²

2.1. Photometric Data

2.1.1. TESS Observations

TOI-1246, also known as TIC 230127302 in the TESS Input Catalog (TIC; Stassun et al. 2018b), was selected for observation at two-minute cadence for a total of 12 sectors in Cycle 2 of the TESS mission (sectors 14–17 and 19–26, 2019 July 18–November 2 and 2019 November 27–2020 July 4). The target lies in TESS’s Northern Continuous Viewing Zone, and was observed for a total of 327 days using either camera 3 or 4. Figure 1 shows the Target Pixel File for TOI-1246 with the TESS aperture and nearby stars identified by Gaia shown for context. Through additional time series observations (see Section 2.1.2), we confirm that the transit events are on-target, and imaging observations indicate that these stars do not significantly contaminate the flux observed (see Section 2.2).

The system is being reobserved for a further 273 days in TESS Cycle 4 in sectors 40–41, 47, and 49–55 (2021 June 24–August 8, 2021 December 30–2022 January 28, 2022 February 26–2022 September 1). TOI-1246 has also been selected for observation at 20 s cadence in Sectors 40 and 41 through the Guest Investigator Programs⁵³ G04039 (PI: Davenport) and G04242 (PI: Mayo). These continued observations will extend the photometric baseline to a total of 1141 days. We make use of TESS photometric data up to and including sector 41 in this

work, and will analyze the additional TESS data in a future work.

The four transiting planets in this system were initially detected by the SPOC pipeline (Jenkins et al. 2016) and released as TOIs on 2019 October 17 (for TOI-1246 b and d) and 2019 November 15 (TOI-1246 c). TOI-1246 e ($P = 37.92 \text{ days}$) was labeled as a Community TOI known as CTOI 230127302 e by Martti Holst Kristiansen⁵⁴ (Brorfelde Observatory, Denmark) before being promoted to a TOI on 2020 July 16.

Figure 2 shows the raw and the normalized and flattened (using a Savitzky–Golay filter; see Savitzky & Golay 1964) photometric light curves for TOI-1246. As of Sector 41, TESS has observed 64 transits of TOI-1246 b, 46 transits of TOI-1246c, 18 transits of TOI-1246 d, and 6 transits of TOI-1246 e; the planet ephemerides suggest that additional transits occurred during gaps in the TESS photometry. We used the PDCSAP_FLUX (Smith et al. 2012; Stumpe et al. 2012, 2014) times series observations in our analysis of this system.

2.1.2. Time Series Observations

We conducted ground-based photometric follow-up observations of TOI-1246 as part of the TESS Follow-up Observing Program⁵⁵ (TFOP; Collins 2019) to confirm the transit-like signals on-target or identify nearby eclipsing binaries (NEBs) as potential sources of the TESS detection. We used the TESS Transit Finder, which is a customized version of the Tapir software package (Jensen 2013), to schedule our transit observations. All photometric data were extracted using AstroImageJ (Collins et al. 2017), except the Dragonfly observations as described below.

We observed a transit egress of TOI-1246 d using the MORAVIAN-G4 9000 camera and the I_c filter on the 0.4 m telescope at the Observatori Astronòmic Albanyà (Girona, Spain). We took these observations on 2020 May 17 UT, and reported a tentative detection of an event that was on-target and in line with the predicted transit depth (measured as $1429 \pm 67 \text{ ppm}$ by TESS). Egress occurred approximately 37 minutes later than predicted (see Section 4.2 for a discussion of TTVs), and we cleared several nearby stars of being NEBs.

We observed a transit of TOI-1246 b using the SBIG STX-16803 + FW-7 camera and the R filter at the George Mason University Observatory on 2019 October 29 between 00:59:34 and 04:50:55 UT. Due to challenging weather conditions and the target’s shallow transit depth (measured as $1104 \pm 46 \text{ ppm}$ by TESS), this observation resulted in a nondetection. However, we ruled out the possibility that one of the nearby stars is an NEB. We observed the target for a total of 231.4 minutes.

We also observed a transit of TOI-1246 b using ASA 1 m f/6 Ritchey–Chrétien telescope, Spectral Instruments 1110S camera and ACE filter wheel/guide camera with the I_c filter at the US Air Force Academy on 2020 March 6 UT. We conclusively detected the transit event with a depth of 0.897 ppt. We note that the observed ingress commenced about 3 minutes later than predicted, and egress ended about 5 minutes early.

We observed another transit of TOI-1246 b using the Las Cumbres Observatory Global Telescope (LCOGT; Brown et al. 2013) 1 m Sinistro instrument at McDonald Observatory on

⁵² ExoFOP (2019), <https://exofop.ipac.caltech.edu/teess/target.php?toi=1246>.

⁵³ <https://heasarc.gsfc.nasa.gov/docs/teess/approved-programs.html#cycle-4>

⁵⁴ ExoFOP (2019), https://exofop.ipac.caltech.edu/teess/view_tag.php?tag=18072.

⁵⁵ <https://tess.mit.edu/followup>

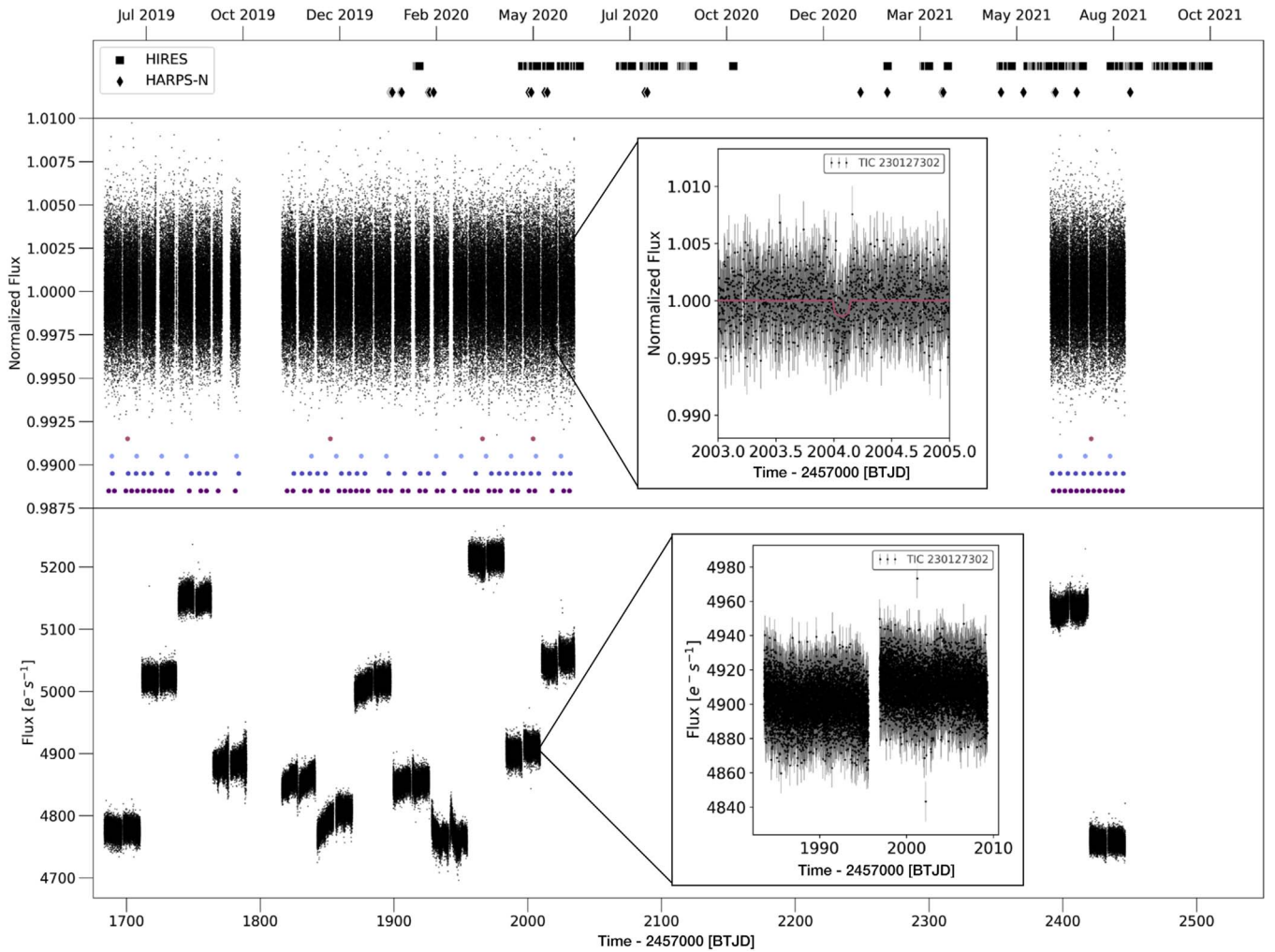


Figure 2. Top panel: the times of Keck/HIRES and TNG/HARPS-N RV observations of TOI-1246, which were contemporaneous with TESS observations. Times are shown in BTJD, which is defined as $\text{BJD}_{\text{TDB}} - 2457000$. BJD_{TDB} is the Barycentric Julian Date in the Barycentric Dynamical Time standard. Middle panel: Flattened and normalized light curve of TOI-1246 derived from TESS PDCSAP photometry using the Lightkurve package (Lightkurve Collaboration et al. 2018). The times of full transits are indicated with dots below the light curve in various colors (TOI-1246 b: purple, TOI-1246 c: blue, TOI-1246 d: light blue, TOI-1246 e: pink). A zoomed-in inset is shown of a single transit of TOI-1246 e with the best-fit model overlaid (see Section 4.1). Lower panel: raw TESS SAP photometry of TOI-1246 with a zoomed-in inset of sector 23 to illustrate intra-sector variability.

2020 May 14 UT. We used the *zs* filter and observed the target for a total of 270 minutes, covering the full transit. The images were calibrated by the standard LCOGT BANZAI pipeline (McCully et al. 2018). These observations confirmed that the transit signal was on-time and on-target.

We observed a fourth transit of TOI-1246 b on 2021 May 28 UT, using the Dragonfly Telephoto Array (DRA). The DRA, housed at the New Mexico Skies telescope hosting facility, is a remote telescope consisting of an array of small telephoto lenses roughly equivalent to a 1.0 m refractor (Danieli et al. 2020). DRA has a SBIG STF-8300M detector with a $156' \times 114'$ field of view. Simultaneous observations of TOI-1246 were conducted in *g'* and *r'* bands with 44 s exposure times. We observed the target for 134 minutes pretransit, 131 minutes in transit, and for 97 minutes posttransit. The data were reduced and analyzed with a custom differential aperture photometry pipeline designed for multi-image processing and analysis. We observed the full transit and made a marginal detection of an on-time and on-target transit, and we report two contaminating sources that are fainter by 3.81 and 6.65 magnitudes, respectively.

We observed a transit of TOI-1246c using the FLI 16803 camera and *Ic* filter at Adams Observatory on 2020 July 14 UT. We used an exposure time of 180 s and observed the target for 241 minutes. We were unable to detect the transit signal on-target, due to the shallow transit depth, but we cleared two nearby stars of being NEBs.

2.2. Imaging Observations

2.2.1. Speckle and Lucky Observations

Stars with small projected separations from an exoplanet host star can create a false-positive transit signal. In addition, “third-light” flux from the close companion star can lead to an underestimated planetary radius, an incorrect mean density, and imprecise stellar parameters (see Ciardi et al. 2015; Furlan et al. 2017). The glare from a close companion can also cause a nondetection of the transits of small planets residing within the same system (Lester et al. 2021). Thus, to search for close-in companions unresolved in TESS or other ground-based follow-up observations, we obtained high-resolution imaging observations of TOI-1246.

TOI-1246 was observed on 2021 June 25 UT using the ‘Alopeke speckle instrument on the Gemini North 8 m telescope (Scott et al. 2021). ‘Alopeke provides simultaneous speckle imaging in two bands (562 nm and 832 nm) and produced a reconstructed image with robust contrast limits on companion detections (e.g., Howell et al. 2016). Seven sets of 1000×0.06 s exposures were collected and subjected to Fourier analysis in our standard reduction pipeline (see Howell et al. 2011). The Fourier transform of the summed autocorrelation of each set of images is used to make a fringe image of the target, which is then used to reconstruct the image. We find that TOI-1246 is a single star with no companion fainter than the target star by 5–7 mag from $0''.1$ to $1''.2$ (i.e., 17–203 au).

We also observed TOI-1246 in the I_c band on 2021 January 24 UT with the Speckle Polarimeter (SPP; Safonov et al. 2017) on the 2.5 m telescope at the Caucasian Observatory of Sternberg Astronomical Institute (SAI) of Lomonosov Moscow State University. SPP uses an Electron Multiplying CCD Andor iXon 897 as a detector, and we used the atmospheric dispersion compensation. The detector has a pixel scale of $20.6 \text{ mas pixel}^{-1}$, the angular resolution is 89 mas, and the field of view is $5'' \times 5''$ centered on the star. The power spectrum was estimated from 4000 frames with 30 ms exposures. We did not detect any stellar companions brighter than $\Delta\text{mag} = 3.8$ and 5.5 at $0''.2$ and $0''.5$, respectively.

Finally, we observed TOI-1246 with the AstraLux instrument (Hormuth et al. 2008) installed at the 2.2 m telescope in the Calar Alto Observatory (Almería, Spain) under average weather and atmospheric conditions (seeing around $1''$) on the night of 2020 February 25 UT with the SDSSz filter. AstraLux uses the lucky imaging technique to obtain thousands of short-exposure frames and then select a few percent of these frames with the best Strehl ratio (Strehl 1902). This process is entirely done by the instrument pipeline. We obtained 95,400 frames with an exposure time of 20 ms each, and we then selected the best 10% for a final effective exposure time of 190.8 s. We used the final stacked image to obtain the contrast curve by using the *astrasens* code (Lillo-Box et al. 2012, 2014). The result provides a contrast of $\Delta z = 5$ mag for separations above $0''.3$ and a maximum contrast of $\Delta z = 3$ mag for $0''.1$. We found no additional sources in the field of view of the instrument ($3'' \times 3''$ in this setup) within these sensitivity limits.

2.2.2. Adaptive Optics Observations

We observed TOI-1246 with the NIRC2 imager (Wizinowich et al. 2000) on the Keck II telescope on 2020 September 28 UT. We took observations in the narrow camera mode (0 d'' pixel^{-1}) with a 1024×1024 pixel FOV, and used a three-point dither pattern to avoid the noisy fourth quadrant of the detector. We used the K filter for a total integration time of 4.5 s and the J filter for a total integration time of 9 s. All of the data were processed and analyzed with a custom set of IDL tools, and the science frames were flat-fielded and sky-subtracted. The sensitivity curve and image resulting from these observations are shown in Figure 3.

We note that there is a proper-motion companion star (TIC 230127303) detected by Gaia that is $4''$ to the NE of TOI-1246. Based on the measured distance of TOI-1246 and this companion (169 pc), these two stars are separated by ~ 750 au. This separation is well within the $21'' \times 21''$ TESS pixels, and so the flux from this companion star affects the photometric light curve for TOI-1246. The companion is 3.8 mag fainter in the

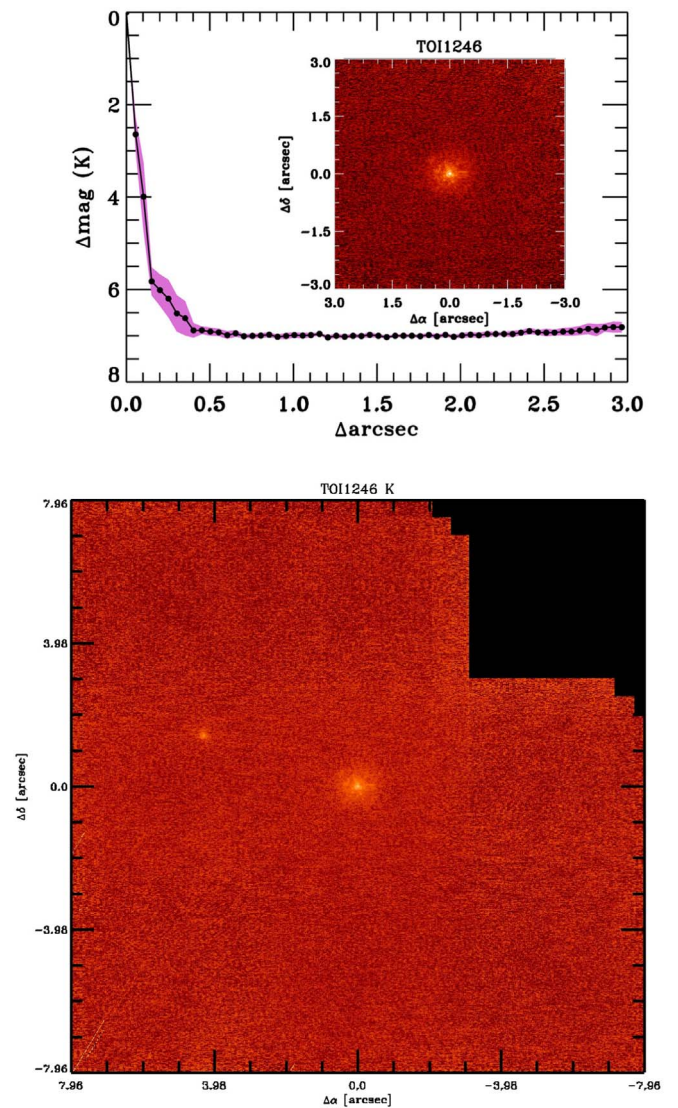


Figure 3. Top: sensitivity curve and zoomed-in image in K band of TOI-1246 using Keck/NIRC2. Bottom: AO image of TOI-1246 using Keck/NIRC2. We see a companion at $\sim 4''$ to the NE of TOI-1246, which does not significantly affect our analysis.

TESS bandpass (magnitudes sourced from the TIC; see Stassun et al. 2018b), and implies a radius correction factor of 1.015 following Furlan et al. (2017). This is smaller than the errors associated with our derived radii (see Section 4.1), and so does not affect our conclusions. Furthermore, this stellar companion does not cause a detectable trend in the RV data, due to its large separation from TOI-1246 (see Section 4.3 for details).

2.3. Spectroscopic Data

2.3.1. Tillinghast/TRES Spectra

We observed two reconnaissance spectra of TOI-1246 on 20 October 2019 UT and on 20 February 2020 UT with the Tillinghast Reflector Echelle Spectrograph (TRES; Fűrész, G 2008) located at the Fred Lawrence Whipple Observatory (FLWO) in Arizona, USA. TRES is a fiber-fed spectrograph with a resolving power of 44,000. The spectra were extracted as described in Buchhave et al. (2010) and were then cross-correlated, order by order, against each

Table 1
TOI-1246 Stellar Parameters

Parameter	Value	Error	Source	Adopted?
Other Names	TIC 230127302, TYC 4423-02107-1 Gaia DR2 1650110904522335744		TIC Stassun et al. (2018b) TYCHO Høg et al. (2000) Gaia DR2 Gaia Collaboration (2018)	...
R.A. (hh:mm:ss)	16:44:27.81		TIC v8.2	...
decl. (hh:mm:ss)	+70:25:47.97		TIC v8.2	...
<i>V</i> magnitude	11.632	0.024	TIC v8.2	...
TESS magnitude	11.1802	0.0061	TIC v8.2	...
<i>J</i> magnitude	10.294		TIC v8.2	...
<i>K</i> magnitude	9.907	0.036	TIC v8.2	...
Gaia magnitude	11.7248	0.0002	Gaia DR2 (Gaia Collaboration 2018)	...
Parallax (mas)	5.847	0.011	Gaia DR2 (Gaia Collaboration 2018)	...
R.A. proper motion (mas/yr)	−48.024	0.047	Gaia DR2 (Gaia Collaboration 2018)	...
decl. proper motion (mas/yr)	81.928	0.051	Gaia DR2 (Gaia Collaboration 2018)	...
Radius (R_{\odot})	0.86	0.05	SpecMatch-Synthetic (Petigura et al. 2017)	Y
Radius (R_{\odot})	0.895	0.038	Calculated using F_{bol} , T_{eff} , and parallax	...
Radius (R_{\odot})	0.876	0.051	TIC v8.2	...
Mass (M_{\odot})	0.87	0.03	SpecMatch-Synthetic (Petigura et al. 2017)	Y
Mass (M_{\odot})	0.93	0.05	Calculated using Torres et al. (2010)	...
Mass (M_{\odot})	0.74	0.18	Calculated using $\log(g)$ and R_*	...
Mass (M_{\odot})	0.868	0.105	TIC v8.2	...
Mass (M_{\odot})	1.12	0.16	Photometric Fit (Section 4.1)	...
$T_{\text{eff}}(K)$	5141	122	TIC v8.2	...
$T_{\text{eff}}(K)$	5151	100	SpecMatch-Synthetic (Petigura et al. 2017)	Y
$T_{\text{eff}}(K)$	5217	50	SPC (Buchhave et al. 2012)	...
$\log(g)$	4.4	0.1	SpecMatch-Synthetic (Petigura et al. 2017)	Y
$\log(g)$	4.53	0.10	SPC (Buchhave et al. 2012)	...
$v \sin i (\text{km s}^{-1})$	1.0	1.0	SpecMatch-Synthetic	Y
$v \sin i (\text{km s}^{-1})$	1.4	0.5	SPC (Buchhave et al. 2012)	...
$P_{\text{rot}}(d)$	47	3	Calculated using Mamajek & Hillenbrand (2008)	...
$P_{\text{rot}} / \sin(i)(d)$	42	40	Calculated using $v \sin i$ and R_*	...
$P_{\text{rot}}(d)$	38	$^{+7}_{-14}$	Calculated using Claytor et al. (2020)	Y
[Fe/H] (dex)	0.17	0.06	SpecMatch-Synthetic (Petigura et al. 2017)	Y
[M/H] (dex)	0.17	0.08	SPC (Buchhave et al. 2012)	Y

other, using the strongest observation as a template. This multi-order analysis revealed a velocity variation of 27 m s^{-1} between the two spectra, similar to the uncertainty of the measurement. We found no significant velocity variation between the two observations, indicating the star is well-suited for precise RV observations. We also derived stellar parameters using the Stellar Parameter Classification (SPC; Buchhave et al. 2012) tool. SPC cross-correlates an observed spectrum against a grid of synthetic spectra based on Kurucz atmospheric models (Kurucz 1992). The weighted average results derived with T_{eff} , $\log(g)$, [M/H], and $v \sin i$ as free parameters are reported in Table 1.

2.3.2. Keck/HIRES Spectra

TKS obtained high-resolution spectra of TOI-1246 using the HIRES spectrograph on the Keck I telescope on Maunakea. We collected 100 spectra between 2019 November and 2021 October. HIRES operates between 360 and 800 nm, and TOI-1246 was observed using the red cross-disperser, C2 decker ($14'' \times 0''.861$, $R = 60,000$), and with a median exposure time of 1004 s. The 100 RV observations were taken with a warm (50°C) iodine cell in the light path for wavelength calibrations

as per Butler et al. (1996). Two further higher-resolution spectra were taken without the iodine cell in the light path (“iodine-out”) in November 2019 and June 2020, in order to obtain a spectral template, using the B3 decker ($14'' \times 0''.574$, $R = 72,000$). The spectra were reduced using the standard procedures described in Howard et al. (2010). The RVs, RV errors, and Mount Wilson S-Index (a proxy for stellar activity derived from Ca II H & K lines; see, e.g., Isaacson & Fischer 2010) values collected on Keck/HIRES are reported in Table 2.

2.3.3. TNG/HARPS-N Spectra

A further 28 high-resolution spectra of TOI-1246 were collected using the HARPS-N instrument installed at the Telescopio Nazionale Galileo (TNG) of Roque de los Muchachos Observatory in La Palma, Spain.⁵⁶ These observations were taken between 2020 February and 2021 September.

⁵⁶ Thirteen spectra were obtained from the Spanish CAT19A_162 program (PI: Nowak), seven spectra from ITP19_1 program (PI: Pallé) and nine spectra from CAT21A_119 program (PI: Nowak).

Table 2
RVs and Spectral Activity Indicators Measured from Keck/HIRES and TNG/HARPS-N

Time (BJD _{TDB})	RV (m s ⁻¹)	RV Unc. (m s ⁻¹)	S index	S Unc.	Instrument
2458917.0623	4.6671	1.7863	0.1336	0.0010	HIRES
2458918.0658	8.9729	1.6653	0.1505	0.0010	HIRES
2458919.0551	0.5704	1.5308	0.1527	0.0010	HIRES
2458995.8758	5.9488	1.9148	0.1480	0.0010	HIRES
2458999.8927	15.7512	1.7060	0.1524	0.0010	HIRES
2459002.9282	3.3317	1.6117	0.1468	0.0010	HIRES
2459003.8913	0.6774	1.5635	0.1430	0.0010	HIRES
2459006.8841	-3.7627	1.6187	0.1448	0.0010	HIRES
2459013.8732	-3.1443	1.6608	0.1465	0.0010	HIRES
2459016.8749	-4.0037	1.8443	0.1479	0.0010	HIRES
2459024.8693	-2.0563	1.6039	0.1303	0.0010	HIRES
2459027.8384	-3.0241	1.3825	0.1461	0.0010	HIRES
2459030.8929	3.0806	1.6265	0.1492	0.0010	HIRES
2459034.8557	6.1822	1.6041	0.1492	0.0010	HIRES
2459036.7920	4.8777	1.4543	0.1466	0.0010	HIRES
2459038.8405	0.2686	1.5753	0.1512	0.0010	HIRES
2459069.0098	5.4160	2.5534	0.1240	0.0010	HIRES
2459071.9366	5.9474	1.7575	0.1447	0.0010	HIRES
2459072.8800	7.4601	1.7438	0.1478	0.0010	HIRES
2459077.8834	11.5812	1.6499	0.1402	0.0010	HIRES
2459086.8748	-9.1120	2.2852	0.0948	0.0010	HIRES
2459089.8754	0.7513	1.6082	0.1397	0.0010	HIRES
2459090.8077	-0.0182	1.6396	0.1532	0.0010	HIRES
2459091.8104	-10.2708	1.6802	0.1496	0.0010	HIRES
2459092.8046	-6.7398	1.5881	0.1521	0.0010	HIRES
2459094.7903	3.0606	1.8001	0.1478	0.0010	HIRES
2459097.8740	-3.7399	1.8511	0.1466	0.0010	HIRES
2459101.7734	0.7005	1.5959	0.1514	0.0010	HIRES
2459114.7515	-2.8354	1.6032	0.1556	0.0010	HIRES
2459115.7854	0.6398	1.5584	0.1394	0.0010	HIRES
2459117.7538	-1.5928	1.5953	0.1579	0.0010	HIRES
2459118.7697	1.9755	1.5657	0.1563	0.0010	HIRES
2459119.7620	-3.0504	1.9919	0.1509	0.0010	HIRES
2459120.7379	-0.0511	1.7190	0.1466	0.0010	HIRES
2459121.7300	-13.9248	1.7669	0.1520	0.0010	HIRES
2459122.7450	-7.8657	1.5958	0.1537	0.0010	HIRES
2459123.7347	0.1256	1.6022	0.1497	0.0010	HIRES
2459153.7107	7.9963	1.6877	0.1355	0.0010	HIRES
2459269.1356	-12.3450	1.7423	0.1277	0.0010	HIRES
2459296.1010	6.7841	1.5442	0.1659	0.0010	HIRES
2459297.0478	3.1049	1.6319	0.1519	0.0010	HIRES
2459300.0061	-4.1661	1.9683	0.1603	0.0010	HIRES
2459314.0783	-1.3336	1.4255	0.1637	0.0010	HIRES
2459353.8600	6.1707	1.6943	0.1601	0.0010	HIRES
2459354.9439	6.4694	1.6786	0.1557	0.0010	HIRES
2459358.9110	-9.5293	1.6953	0.1541	0.0010	HIRES
2459361.9457	8.0640	1.4567	0.1597	0.0010	HIRES
2459373.8191	6.6260	1.6829	0.1592	0.0010	HIRES
2459377.0715	-5.2521	1.5642	0.1455	0.0010	HIRES
2459377.8308	5.2305	1.6516	0.1611	0.0010	HIRES
2459378.8909	5.2943	1.4859	0.1599	0.0010	HIRES
2459379.9073	-6.2703	1.6647	0.1617	0.0010	HIRES
2459383.0151	0.9678	1.6524	0.1595	0.0010	HIRES
2459383.9827	2.8946	1.6310	0.1536	0.0010	HIRES
2459385.8374	-8.5394	1.6133	0.1542	0.0010	HIRES
2459388.0531	-3.7768	1.6463	0.1522	0.0010	HIRES
2459388.9024	-10.0083	1.6023	0.1649	0.0010	HIRES
2459389.8761	-12.9257	1.5479	0.1585	0.0010	HIRES
2459395.9321	-4.7191	1.5397	0.1573	0.0010	HIRES
2459399.8640	-9.5533	1.7150	0.1601	0.0010	HIRES
2459404.9747	-2.2866	1.4522	0.1535	0.0010	HIRES
2459406.8859	-9.5983	1.6463	0.1559	0.0010	HIRES
2459407.9203	-0.8518	1.8118	0.0000	0.0010	HIRES
2459408.9688	4.6775	1.5936	0.1521	0.0010	HIRES
2459409.9706	-1.8515	1.7468	0.1539	0.0010	HIRES

Table 2
(Continued)

Time (BJD _{TDB})	RV (m s ⁻¹)	RV Unc. (m s ⁻¹)	S index	S Unc.	Instrument
2459412.9687	3.5893	1.5592	0.1542	0.0010	HIRES
2459413.9763	5.0963	2.2444	0.1394	0.0010	HIRES
2459414.9853	4.5878	2.6134	0.1410	0.0010	HIRES
2459435.7827	3.1791	1.6335	0.1554	0.0010	HIRES
2459441.8991	2.8895	1.6247	0.1604	0.0010	HIRES
2459444.9312	6.0879	1.6149	0.1580	0.0010	HIRES
2459448.8678	10.8938	1.9052	0.1563	0.0010	HIRES
2459449.8081	7.5028	1.6172	0.1598	0.0010	HIRES
2459450.8254	1.0285	1.7628	0.1448	0.0010	HIRES
2459451.8711	9.3126	1.6446	0.1652	0.0010	HIRES
2459452.8133	6.6857	1.5619	0.1581	0.0010	HIRES
2459455.7976	7.1597	1.5236	0.1641	0.0010	HIRES
2459456.8270	3.4921	1.6717	0.1673	0.0010	HIRES
2459469.7871	-6.1427	1.6299	0.1604	0.0010	HIRES
2459470.7829	-5.3842	1.6701	0.1623	0.0010	HIRES
2459472.7681	-3.8466	1.6613	0.1483	0.0010	HIRES
2459475.7760	-17.8983	1.8216	0.1581	0.0010	HIRES
2459476.7713	-10.8095	1.6625	0.1597	0.0010	HIRES
2459478.7999	0.7152	1.7799	0.1648	0.0010	HIRES
2459482.7845	-2.5158	1.5947	0.1629	0.0010	HIRES
2459483.7797	0.8174	1.6887	0.1588	0.0010	HIRES
2459484.7623	-1.0387	1.6102	0.1554	0.0010	HIRES
2459489.7755	-3.6559	1.7329	0.1475	0.0010	HIRES
2459497.7223	-5.6037	2.1168	0.1585	0.0010	HIRES
2459498.7418	-5.0932	1.9443	0.1624	0.0010	HIRES
2459502.7756	5.0014	1.7797	0.1572	0.0010	HIRES
2459503.7694	4.7857	1.8185	0.1497	0.0010	HIRES
2459504.7741	-12.2155	1.8252	0.1666	0.0010	HIRES
2459506.7250	-3.0769	1.8514	0.1676	0.0010	HIRES
2459508.7248	3.8190	1.7255	0.1642	0.0010	HIRES
2459513.7437	1.5101	1.7032	0.1223	0.0010	HIRES
2459516.7123	3.2775	1.8132	0.1641	0.0010	HIRES
2459622.1271	-0.5991	1.8356	0.1579	0.0010	HIRES
2459626.1265	-1.3294	1.7349	0.1516	0.0010	HIRES
2459632.1152	7.7221	1.6469	0.1643	0.0010	HIRES
2458896.7475	4.5793	2.1153	0.1760	0.0126	HARPS-N
2458897.7587	0.6066	1.7459	0.1624	0.0093	HARPS-N
2458898.7442	-0.3685	1.6674	0.1663	0.0101	HARPS-N
2458904.7360	3.8349	1.6534	0.1397	0.0096	HARPS-N
2458905.7339	10.4724	1.5069	0.1617	0.0057	HARPS-N
2458925.7178	5.6357	1.7037	0.1601	0.0076	HARPS-N
2458926.7187	9.6815	1.3208	0.1559	0.0056	HARPS-N
2458929.7005	9.5106	1.1660	0.1508	0.0047	HARPS-N
2459000.5461	11.8829	1.3999	0.1638	0.0074	HARPS-N
2459000.6312	14.3818	1.4844	0.1728	0.0084	HARPS-N
2459002.5486	-0.3836	1.0787	0.1681	0.0044	HARPS-N
2459002.6361	-2.5666	1.2797	0.1719	0.0052	HARPS-N
2459012.5520	-0.9495	1.3709	0.1633	0.0067	HARPS-N
2459012.6414	-1.3279	1.1019	0.1626	0.0050	HARPS-N
2459014.6408	-9.3870	1.4438	0.1606	0.0066	HARPS-N
2459087.3945	-6.0197	1.7265	0.1731	0.0105	HARPS-N
2459089.3867	-3.9607	2.5947	0.1394	0.0192	HARPS-N
2459248.7604	5.5201	1.3695	0.1714	0.0067	HARPS-N
2459268.7188	-7.4858	2.4539	0.1824	0.0180	HARPS-N
2459309.6076	1.4668	1.8518	0.1718	0.0091	HARPS-N
2459310.6164	-2.3908	2.2873	0.1684	0.0151	HARPS-N
2459353.6993	5.6099	2.0655	0.1632	0.0166	HARPS-N
2459353.7169	3.8382	1.9814	0.1673	0.0158	HARPS-N
2459370.5405	2.1340	2.4140	0.1647	0.0169	HARPS-N
2459393.6381	-11.8390	1.3336	0.1672	0.0070	HARPS-N
2459394.5373	-10.6052	1.5538	0.1824	0.0095	HARPS-N
2459410.4726	4.9166	2.1437	0.1900	0.0133	HARPS-N
2459450.4350	7.3945	1.3333	0.1726	0.0064	HARPS-N

The exposure time was set to 1800–3600 s, based on weather conditions and scheduling constraints, leading to a signal-to-noise ratio per pixel of 25–56 at 5500 Å. We used the `serval` code (Zechmeister et al. 2018) to measure relative RVs by template-matching, and also to derive the chromatic index (CRX), differential line width (dLW), H α , and sodium Na D1 & Na D2 indices. Doppler measurements and spectral activity indicators (CCF_FWHM, CCF_CTR, BIS, and Mount Wilson S-index) were measured using an online version of the DRS, the YABI tool,⁵⁷ by cross-correlating the extracted spectra with a K5 mask (Baranne et al. 1996). The RVs, RV errors, and values of the Mount Wilson S-Index collected on TNG/HARPS-N are reported in Table 2.

3. Stellar Parameters

We used several methods to characterize TOI-1246. We report these values in Table 1, and indicate with asterisks the preferred values that we used where multiple values were obtained for a given parameter (we note that the multiple values are consistent). We used the `SpecMatch-Synthetic`⁵⁸ code (Petigura et al. 2017) to fit sections of the iodine-out optical spectrum collected with Keck/HIRES using forward modeling by interpolating between a grid of model spectra from Coelho et al. (2005). We use this method to derive the effective temperature ($T_{\text{eff}} = 5151 \pm 100$ K), stellar radius ($R_* = 0.86 \pm 0.05 R_\odot$), surface gravity ($\log(g) = 4.4 \pm 0.1$), and metallicity ($[\text{Fe}/\text{H}] = 0.17 \pm 0.06$) of TOI-1246.

We also analyzed the broadband spectral energy distribution (SED) of the star together with the Gaia EDR3 parallax (with no systematic offset applied; see, e.g., Stassun & Torres 2021), in order to measure the stellar radius, following the procedures described in Stassun & Torres (2016), Stassun et al. (2017), and Stassun et al. (2018a). We obtained the B , V magnitudes from APASS, the J , H , K_S magnitudes from 2MASS, the $W1$ – $W4$ magnitudes from WISE, the G_{BP} , G_{RP} magnitudes from Gaia, and the NUV magnitude from GALEX. The available photometry spans the full stellar SED from 0.2 to 22 μm (see Figure 4).

We performed a fit using Kurucz stellar atmospheric models (Kurucz 1993), with the effective temperature (T_{eff}), metallicity ($[\text{Fe}/\text{H}]$), and surface gravity ($\log(g)$) adopted from the spectroscopic analysis. The remaining free parameter is the extinction A_V , which we limited to the maximum line-of-sight value from the Galactic dust maps of Schlegel et al. (1998). The resulting fit has a best-fit $A_V = 0.11 \pm 0.02$ and a reduced χ^2 of 2.7, but we note that the GALEX NUV flux indicates a moderate level of activity. Integrating the (unreddened) model SED gave the bolometric flux at Earth, $F_{\text{bol}} = 5.56 \pm 0.20 \times 10^{-10} \text{ erg s}^{-1} \text{ cm}^{-2}$. Taking the F_{bol} and T_{eff} together with the Gaia parallax, we derived a stellar radius, $R_* = 0.895 \pm 0.08 R_\odot$. In addition, we estimated the stellar mass from the empirical relations of Torres et al. (2010), giving $M_* = 0.93 \pm 0.05 M_\odot$, which is consistent with the estimate of $M_* = 0.74 \pm 0.18 M_\odot$ obtained directly from R_* and the spectroscopic $\log(g)$.

We used the stellar NUV excess (see Figure 4) to estimate a rotation period and age via empirical rotation–activity–age relations. The observed NUV excess implies a chromospheric activity of $\log R'_{\text{HK}} = -4.98 \pm 0.05$ following Findeisen et al. (2011), which is consistent with the $\log R'_{\text{HK}}$ measured with

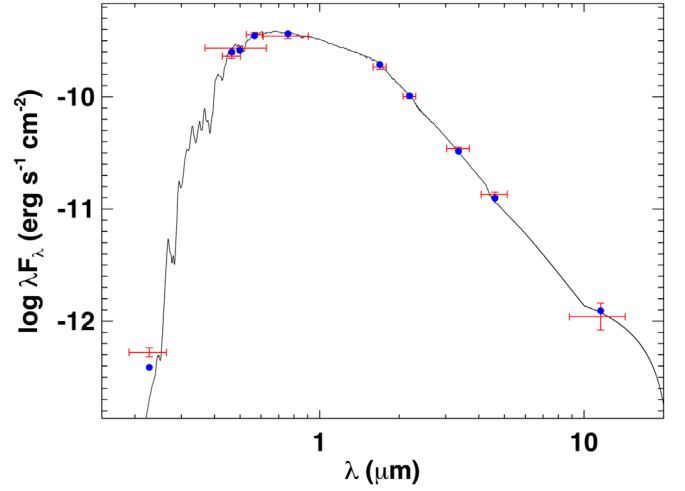


Figure 4. Spectral energy distribution of TOI-1246. Red symbols represent the observed photometric measurements, and the horizontal bars represent the effective width of the passband. Blue symbols are the model fluxes from the best-fit Kurucz atmosphere model (black). We observe some NUV excess that implies moderate stellar activity for this star.

Keck/HIRES ($\log R'_{\text{HK}} = -5.10 \pm 0.15$). We also measured the Mount Wilson S-Index to be 0.150 ± 0.001 using Keck/HIRES, which indicates low chromospheric activity (Wilson 1978). The $\log R'_{\text{HK}}$ value implies a stellar rotation period of $P_{\text{rot}} = 47 \pm 3$ d according to the empirical relations of Mamajek & Hillenbrand (2008). However, the values of $\log R'_{\text{HK}}$ and $B-V$ (0.943) found for TOI-1246 are at the edge of (or beyond) the range considered in Mamajek & Hillenbrand (2008; $\log R'_{\text{HK}} < -5$, and $0.5 < B - V < 0.9$), and so the uncertainty is likely underestimated. The NUV estimated activity also implies an age of 6.2 ± 0.8 Gyr via the empirical relations of Mamajek & Hillenbrand (2008), but this error is also likely underestimated.

We also attempted to obtain a rotation period measurement directly from the data. We first performed a uninformed search for stellar rotation in the TESS 2 and 30 minute cadence light curves. We could find no convincing rotation period using a Lomb–Scargle periodogram (Lomb 1976; Scargle 1982), autocorrelation function (McQuillan et al. 2013), or wavelet decomposition (Torrence & Compo 1998; Mathur et al. 2010). However, rotation periods longer than 13.7 days have eluded detection in TESS light curves, due to the 27 day sector length and thermal effects on the detector sensitivity related to the data downlink at the midpoint of each sector (e.g., Canto Martins et al. 2020; Avallone et al. 2021). Therefore, we passed the light curve’s wavelet decomposition through the convolutional neural network of Claytor et al. (2022). The neural network is trained using wavelet decomposition of simulated rotational light curves with real TESS systematics and noise. Given an input image of the wavelet transform, the neural network predicts a rotation period and a heuristic (but not statistical) uncertainty. Based on ensemble recovery, if the uncertainty is less than about 35% of the predicted period, the period is likely to be real. We found no reliable rotation period with this method.

In the absence of photometric rotation signatures, we put theoretical constraints on the stellar rotation period using the stellar model-fitting tools in `kiauhoku` (Claytor et al. 2020). We used an MCMC routine to fit the models of van Saders & Pinsonneault (2013) and van Saders et al. (2016) to the star’s

⁵⁷ Available at <http://ia2-harps.oats.inaf.it:8000>.

⁵⁸ github.com/petigura/specmatch-syn

effective temperature, metallicity, and surface gravity, yielding rotation period predictions following three different braking laws. The different braking laws vary combinations of starting condition and stalled braking behavior at a critical Rossby number (van Saders et al. 2016). Regardless of the braking law used, we predicted a rotation period of 38_{-14}^{+7} d for TOI-1246, which is consistent with the prediction from Mamajek & Hillenbrand (2008). Both results are consistent with the rotation period estimate from the spectroscopic $v_{\sin(i)}$ and R_* of 42 ± 40 days, due to the large error on $v_{\sin(i)}$. Overall, TOI-1246 is a relatively old, low-activity, and slightly metal-rich K dwarf.

4. Data Analysis

4.1. Photometric Fit

We first performed an MCMC fit of the TESS photometry using the *emcee* package (Foreman-Mackey et al. 2013) for each of the four transiting planets. We used the planet radii, periods, and transit times reported by the TOI catalog (Guerrero et al. 2021) to initiate *batman* (Kreidberg 2015) transit models. We set planet eccentricities and arguments of periastron to zero for simplicity, and used Kepler’s Third Law to calculate an initial guess for the semimajor axes of the planets. Based on the effective temperature, $\log(g)$, and metallicity of TOI-1246, we adopt test values of $u_1 = 0.1$ and $u_2 = 0.4$ for quadratic limb darkening parameters following Claret (2017). We used 48 walkers, and varied the following parameters for each planet: transit time, orbital period, planet radius, semimajor axis, and inclination. We assessed convergence using the integrated autocorrelation time.

Using the results of the initial MCMC analysis and using the stellar parameters derived in Section 3 as priors, we then performed a joint photometric fit of the four planets using the *exoplanet* package (Foreman-Mackey et al. 2020). The photometric fit included a total of 21 free parameters. Each planet had four free parameters: orbital period (P), epoch (T_0), planet radius relative to stellar radius (R_p/R_*), and impact parameter (b). There are five further global parameters: quadratic limb darkening parameters (u_1 , u_2), stellar mass (M_*) and radius (R_*), and a mean flux value (μ). We assumed planet eccentricities to be 0 (motivated in Section 4.3). We chose to use epochs roughly halfway through the overall photometric baseline in order to speed up the photometric fit and reduce rounding errors. We calculated the transit times by assuming a linear ephemeris and propagating the transit midpoint time forward to near 2459000 BJD_{TDB}. The resulting planet radii are consistent with the radii found by the SPOC pipeline.

However, individual analyses of the system’s transits, in particular those of the outermost planet 1246 e, showed some notable discrepancies with our transit models. There was non-negligible structure in the out-of-transit flux baseline, and the modeled ingresses and egresses of TOI-1246 e and d were somewhat discrepant from the data. We attempted to “whiten” the photometry and smooth out short-timescale stellar activity by applying a Gaussian Process (GP) in addition to the transit fits (Foreman-Mackey et al. 2017). We used the Simple Harmonic Oscillator (SHO) kernel built into the *exoplanet* package (Foreman-Mackey et al. 2020). We varied two hyperparameters: ρ , with a log normal prior with $\mu_\rho = 0$ and $\sigma_\rho = 10$; and σ , with a log normal prior with a mean equal to

the standard deviation of the light curve flux, and a standard deviation of 10. We hold the final hyperparameter fixed, with a value of $Q = \frac{1}{\sqrt{2}}$. While there was some modest improvement, much of the structure remained after such a fit.

We thus concluded that the poor fit of our model for TOI-1246 d and e was due to unmodeled TTVs. Therefore, we performed a TTV analysis with the Python Tool for Transit Variations (PyTTV) that models the transits using *Pytransit* (Parviainen 2015) and the stellar variability as a GP with a matern 3/2 kernel using *celerite* (Foreman-Mackey et al. 2017). This fit included the following free parameters: orbital period (P), epoch (t_0), planet radius relative to stellar radius (R_p/R_*), transit midpoints (t_c), and impact parameter (b) for all four planets, while stellar density, and the quadratic limb darkening parameters (u_1 , u_2) were shared for all the planets. The transits from all the planets in the TOI-1246 system were fit jointly by modeling them with the quadratic Mandel & Agol (2002) transit model implemented in *Pytransit* via a Taylor-series expansion (Parviainen & Korth 2020). Section 4.2 describes the measured TTVs in more detail. We estimated the model parameter posteriors using MCMC-sampling (*emcee*; Foreman-Mackey et al. 2013), and found that the transit midpoints show variations from a linear ephemeris. We show the phase-folded transits accounting for the TTVs in Figure 5, and calculate the following radii: $R_b = 2.97 \pm 0.06 R_\oplus$, $R_c = 2.47 \pm 0.08 R_\oplus$, $R_d = 3.46 \pm 0.09 R_\oplus$, and $R_e = 3.72 \pm 0.16 R_\oplus$. We also derive a stellar density of $2.47 \pm 0.25 \text{ g cm}^{-3}$. This corresponds to a stellar mass of $1.12 \pm 0.16 M_\odot$, which is consistent with values in Table 1. We apply the radius correction factor of 1.015 calculated in Section 2.2.2, and report the final planet radii and other system parameters in Table 3.

Alongside the fits described above, we also fit the TESS photometry using the TATER code (C. F. Harada et al., 2022, in preparation). TATER (the Tess trAnsiT fITTER) is a custom Python tool that applies the Transit Least Squares (TLS; Hippke & Heller 2019) algorithm to TESS photometry accessed via the *Lightcurve* package (*Lightcurve* Collaboration et al. 2018) to iteratively search for transit signals, and it implements an MCMC sampler to determine a best-fit *batman* transit model (Kreidberg 2015) for each significant detection. TATER successfully recovered four transit signals consistent with the preferred fits for TOI-1246 b, TOI-1246c, TOI-1246 d, and TOI-1246 e. It did not identify any significant transit signals at periods longer than that of TOI-1246 e and shorter than ~ 250 days. The current photometric baseline of TESS observations is 752 days, with a large data gap, so a planet with an orbital period $\lesssim 250$ days could transit three times in the light curve. This suggests that the system lacks additional longer-period transiting planets with radii similar to those of the known transiting planets.

4.2. Anticipated and Observed Transit-timing Variations

A subset of transiting planets in multiplanet systems are amenable to mass measurements using the TTV method (Hadden & Lithwick 2017; Agol & Fabrycky 2018). TTVs in systems with only one known transiting planet have also been used to detect additional planets that were not initially detected (e.g., Ballard et al. 2011; Lam et al. 2020). The NASA Exoplanet Archive reports that at least 325 of the 4531 confirmed planets display TTVs (as of 2021 November 5). The TESS mission was predicted to find ~ 90 systems that exhibit TTVs during its prime and extended mission (Hadden et al. 2019). The NASA

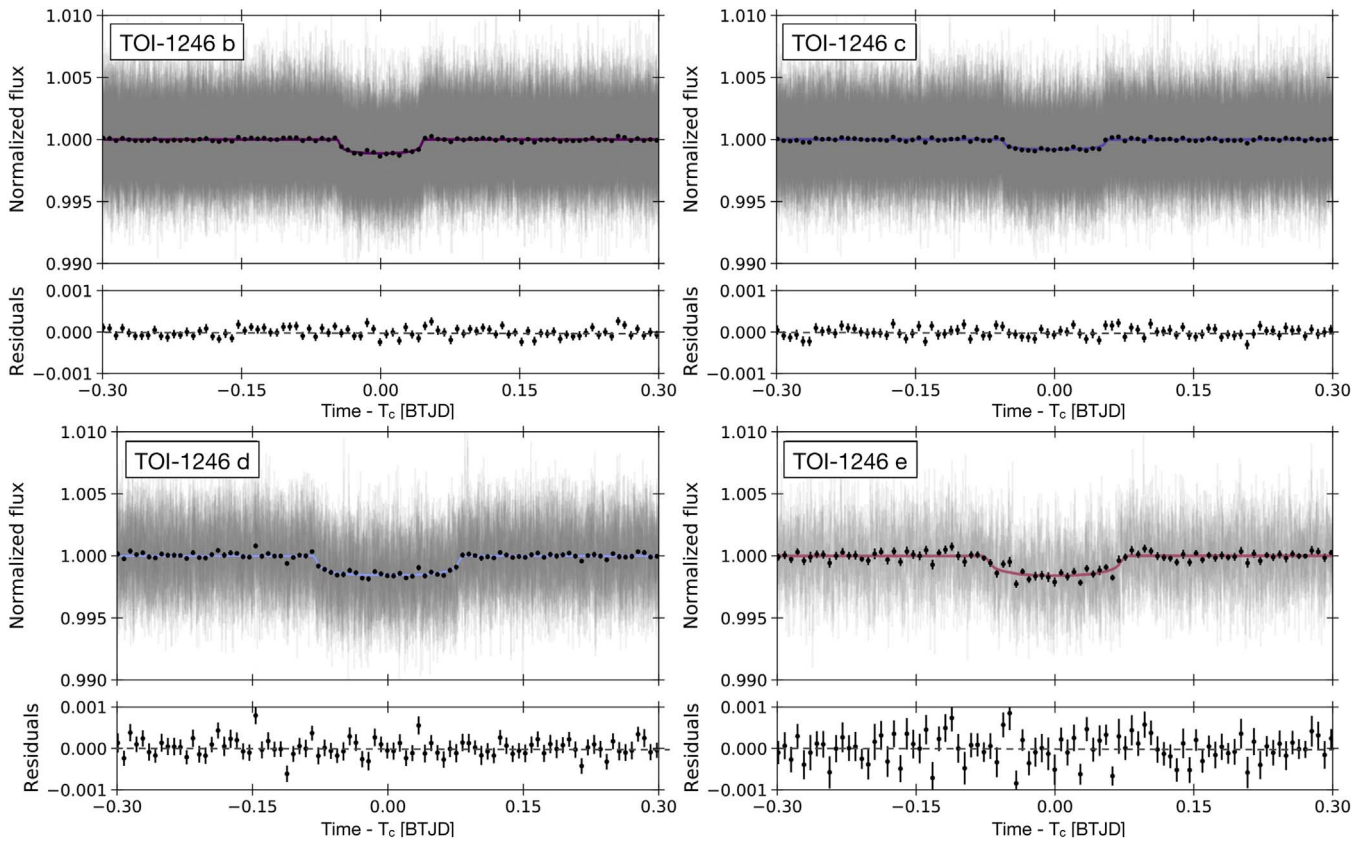


Figure 5. TESS light curves phased at the orbital periods of the four transiting planets. Gray data are individual data points, black data points are binned data, and the overlaid curves are our best-fit GP and TTV model (TOI-1246 b: purple, TOI-1246c: blue, TOI-1246 d: light blue, TOI-1246 e: pink). Residuals are shown beneath each plot.

Exoplanet Archive reports that five TESS confirmed planets exhibit TTVs (as of 2021 November 5).

TOI-1246 d ($P = 18.66$ days) and TOI-1246 e ($P = 37.92$ days) lie just exterior to the 2:1 mean-motion resonance, with a period ratio of 2.03. We predicted the magnitude of TTV signals for these planets using the equations laid out in Lithwick et al. (2012). We used the planet masses and periods reported in Table 3, and assumed circular orbits. The estimated magnitude of the TTVs in this system (Lithwick et al. 2012) are 22 minutes for TOI-1246 d (the inner planet of the pair), and 4 minutes for TOI-1246 e. We also calculated the TTV super-period to be $P_{\text{super}} = 1264$ days. The photometric data we analyzed cover 384 days within a time span of 632 days, and so only cover 50% of the super-period. However, an additional 273 days of data will be collected in Cycle 4, leading to an overall baseline of 1141 days. This will increase the coverage of the super-period to around 90%. The upcoming sectors will observe an additional 54 transits of TOI-1246 b, 40 transits of TOI-1246c, 13 transits of TOI-1246 d, and 6 transits of TOI-1246 e. These observations will double the number of observed transits for TOI-1246 e.

As described in Section 4.1, we fit the individual transit midpoints for TOI-1246 d and TOI-1246 e in order to measure TTVs. Figure 6 shows the difference between the observed and calculated transit midpoints. We see clear evidence of TTVs for both planets, and note that they are larger in amplitude than the predicted magnitudes derived from Lithwick et al. (2012). This may be due to the effects of nonzero orbital eccentricities or the effect of a fifth planet candidate in the system (see Section 4.4), which may form a resonant chain with TOI-1246 d and

TOI-1246 e. We do not investigate whether TOI-1246 d and TOI-1246 e are in resonance in this work. We will explore this result further in a follow-up work using the upcoming TESS photometry.

4.3. Radial Velocity Analysis

We performed a fit of the precision radial velocity data collected using Keck/HIRES and TNG/HARPS-N using the *RadVel* package (Fulton et al. 2018). Figure 7 shows the Lomb–Scargle (Lomb 1976; Scargle 1982) periodograms for the RV data.

In our RV analysis, we fixed the linear-ephemeris orbital periods and planet transit times to the values measured from TESS photometry. We restricted the semi-amplitude of each planet (K) to be positive, in order to constrain planet masses >0 , which is physically motivated. For each instrument, we introduce an RV offset term (γ) and an RV jitter term (σ), for a total of four instrumental parameters. We also considered an RV trend term ($\dot{\gamma}$), although our fits preferred values near zero for this parameter. In our simplest model, we assumed circular orbits for the four transiting planets, resulting in nine free parameters: four semi-amplitudes, two jitter parameters, two RV offset parameters, and one RV trend parameter.

We performed several different fits with a variety of eccentricity priors. The most restrictive eccentricity prior used the orbit-crossing eccentricity of each planet (TOI-1246 d: $e_{\text{cross}} = 0.536$, TOI-1246 b: $e_{\text{cross}} = 0.234$, TOI-1246c: $e_{\text{cross}} = 0.1897$, and TOI-1246 e: $e_{\text{cross}} = 0.377$) as an upper limit for eccentricity. The orbit-crossing eccentricity is the eccentricity at which the orbit of a planet in the

Table 3
TOI-1246 System Parameters

Parameter	Value	TOI-1246 b		TOI-1246 c		TOI-1246 d		TOI-1246 e		Source
		Value	Error	Value	Error	Value	Error	Value	Error	
Photometric Parameters										
Period (days)		4.30744	0.00002	5.904144	0.000083	18.65590	0.00048	37.9216	0.0010	Photometric Fit
Epoch-2457000 (BTJD)		1686.5658	0.0010	1683.4661	0.0027	1688.9653	0.0090	1700.7134	0.0089	Photometric Fit
Impact parameter, b		0.49	0.07	0.20	0.15	0.29	0.11	0.73	0.04	Photometric Fit
Equilibrium Temperature ^a (K)		955		860		586		462		ExoFOP-TESS
R_p/R_*		0.031	0.001	0.026	0.001	0.036	0.001	0.039	0.002	Photometric Fit
Radius (R_\oplus)		3.01	0.06	2.51	0.08	3.51	0.09	3.78	0.16	From R_p/R_*
Semimajor axis, a (R_*)		13.4	0.5	16.6	0.6	35.7	1.2	57.3	2.0	Photometric Fit
Semimajor axis, a (AU)		0. y	0.002	0.061	0.002	0.131	0.004	0.211	0.007	Photometric Fit
Inclination (deg)		87.9	0.4	89.3	0.5	89.5	0.2	89.3	0.1	From a (R_*), b
Limb darkening, u_1	0.12 ± 0.10									Photometric Fit
Limb darkening, u_2	0.70 ± 0.17									Photometric Fit
Spectroscopic Parameters										
RV Semi-amplitude (m s^{-1})		3.44	0.64	2.99	0.62	1.66	0.64	3.77	0.65	Radvel
HIRES RV Offset (m s^{-1})	2.08 ± 0.70									Radvel
HARPS-N RV Offset (m s^{-1})	4.87 ± 0.85									Radvel
HIRES RV Jitter (m s^{-1})	2.88 ± 0.34									Radvel
HARPS-N RV Jitter (m s^{-1})	3.18 ± 0.60									Radvell
Planet Mass (M_\oplus)		8.1	1.1	8.8	1.2	5.3	1.7	14.8	2.3	Radvel
Density (g cm^{-3})		1.63	0.23	3.21	0.44	0.70	0.23	1.51	0.26	From M_p , R_p
Atmospheric Parameters										
Insolation Flux (F_\oplus)		196		129		28		11		ExoFOP-TESS
Transmission Spectroscopy Metric		48.9	$^{+9.7}_{-7.6}$	22.9	$^{+5.0}_{-3.9}$	72.7	$^{+35.9}_{-19.2}$	24.5	$^{+6.3}_{-4.9}$	Using Kempton et al. (2018)

Note.

^a Assuming a Bond albedo of 0.3.

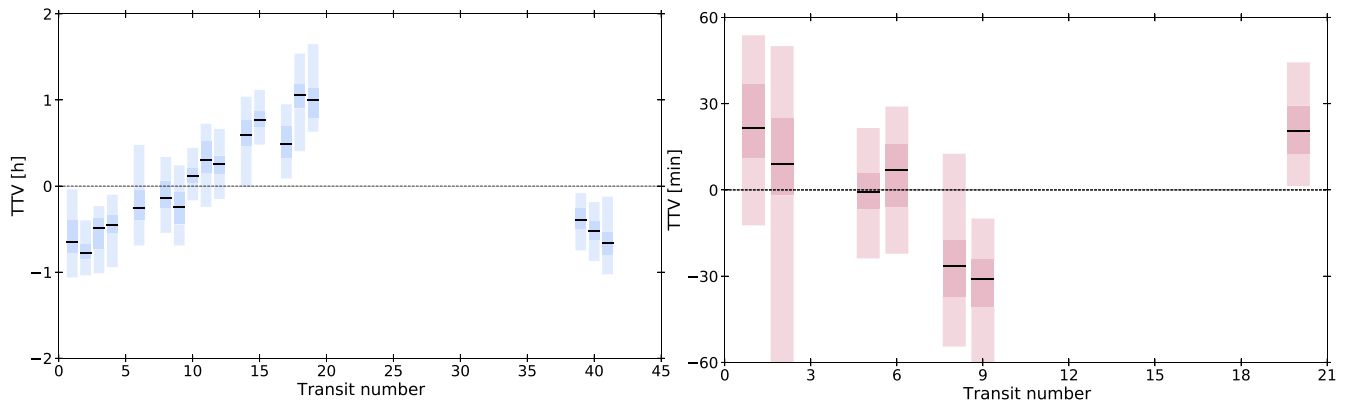


Figure 6. Observed—Computed plots for TOI-1246 d (left) and TOI-1246 e (right). The shaded area of each bar represents the one- and three-sigma standard deviations of each TTV measurement. Both planets show strong evidence of TTVs. Transit number 2 of TOI-1246 e was not fully observed by TESS, leading to a larger error bar on the TTV measurement.

system would cross that of an adjacent planet (assuming the adjacent planet’s orbit is circular). In less restrictive cases, we explored letting eccentricities vary fully from $e = 0$ to $e = 1$ and letting eccentricities vary up to upper limits set by our analysis of system stability. We also performed fits in which the three inner planets had circular orbits and the eccentricity of TOI-1246 e was allowed to vary. Regardless of the specific choice of eccentricity prior, we found that the resulting planet mass estimates remained within the 1σ confidence interval of the circular orbit solutions. We report masses from the circular orbit solutions as motivated below and in Section 4.7. Figure 8 shows both the corresponding global fit and the phased RV model with other planet models subtracted for each planet.

Our decision to adopt the zero-eccentricity fit results is supported by Yee et al. (2021), who investigated a sample of 19 Kepler compact multiplanet systems with precise planet masses and eccentricities measured using TTVs. They found that the planet eccentricities in these systems were significantly (from a few to 10 times) smaller than required for dynamic stability, and even smaller than the orbit-crossing limits. In other words, these systems are overstable, implying that planet eccentricities must be damped if these planets initially formed through giant impacts. TOI-1246 has two planets near resonance that exhibit TTVs, and it is therefore similar to the planet sample considered by Yee et al. (2021). Van Eylen & Albrecht (2015) and Van Eylen et al. (2019) further find that planets in Kepler multiplanet systems tend to have smaller eccentricities than—and have an eccentricity distribution distinct from those of—planets in systems with only one transiting planet detected. These results strengthen our choice to report the results of the zero-eccentricity RV fits.

4.4. A Fifth Periodic Signal in the RV Data

An additional consideration in our analysis is a fifth periodic signal in the RV data with a period longer than that of TOI-1246 e. The Lomb–Scargle periodogram of the RV data residuals from a four-planet model includes signals at both 76.2 d and 93.8 d (see Figure 7). We also computed an l_1 periodogram (Hara et al. 2017) of the RVs. The l_1 periodogram was developed to search for periodic signals in RV data, and aims to reduce the number of peaks due to aliasing when compared to a Lomb–Scargle periodogram. We find evidence of signals at ~ 74 d and ~ 94 d in the l_1 periodogram. To test the robustness of these signals, we performed bootstrap sampling

(Efron 1979) on the residuals from a four-planet RV fit. The signals are robust to bootstrap sampling to $>99.99\%$ confidence, and thus must be considered in our analysis.

4.5. Possible Explanations for the Fifth Signal

It is possible that this fifth Keplerian signal is a result of nonzero eccentricity of TOI-1246 e that is not addressed in our zero-eccentricity RV model. In order to test this possibility, we fit the RV data set with a four-planet model and allow the eccentricity of TOI-1246 e to vary. This model reported an eccentricity of 0.1 ± 0.1 for TOI-1246 e, and does not remove the additional signals seen in the RV residuals between 70 and 100 d. Both the 76 d and 94 d signals remain robust to $>99.99\%$ after bootstrap sampling the RV residuals of this fit. Therefore, we do not consider unmodeled eccentricity as a plausible explanation for this signal.

Another possible explanation is that it is related to stellar activity and rotation. Figure 7 shows that there is a peak in the S-Index Lomb–Scargle periodogram at 80 d, and a peak at 76 d in the HARPS-N BIS periodogram. However, our analysis of the photometric light curve and predictions for the stellar rotation period are inconsistent with a rotation-related signal at either of the two candidate periods with $>99.9\%$ confidence (more details in Section 3). Therefore, we do not believe this signal to be related to star spots modulated by stellar rotation. Furthermore, there are no significant peaks between 70 and 100 d in the CCF_CTR or FWHM spectral activity indicator periodograms derived from HARPS-N data. The signal at 80 d in the S-Index periodogram may arise from the window function (and thus not be astrophysical) or from stellar activity on the timescale of 80 days that our analysis has not sufficiently considered.

Finally, we consider the potential sampling effect of the RV observations. The spectral window function (shown in Figure 7) shows a peak near 90 days, and may be clouding our picture of signals in the 70–100 days range. Furthermore, both the 76.2 d and 93.8 d candidate periods for the fifth signal are near harmonics of other planet periods (TOI-1246 e: $37.92\text{d} \approx 76\text{d}/2$, and TOI-1246 d: $18.66\text{d} \approx 94\text{d}/5$, respectively), and so may appear more significant in the RV periodogram than they actually are, due to aliasing. We are collecting additional RVs using WIYN/NEID in the 2022A observing semester in order to mitigate these aliasing effects resulting from uneven sampling (Dawson & Fabrycky 2010).

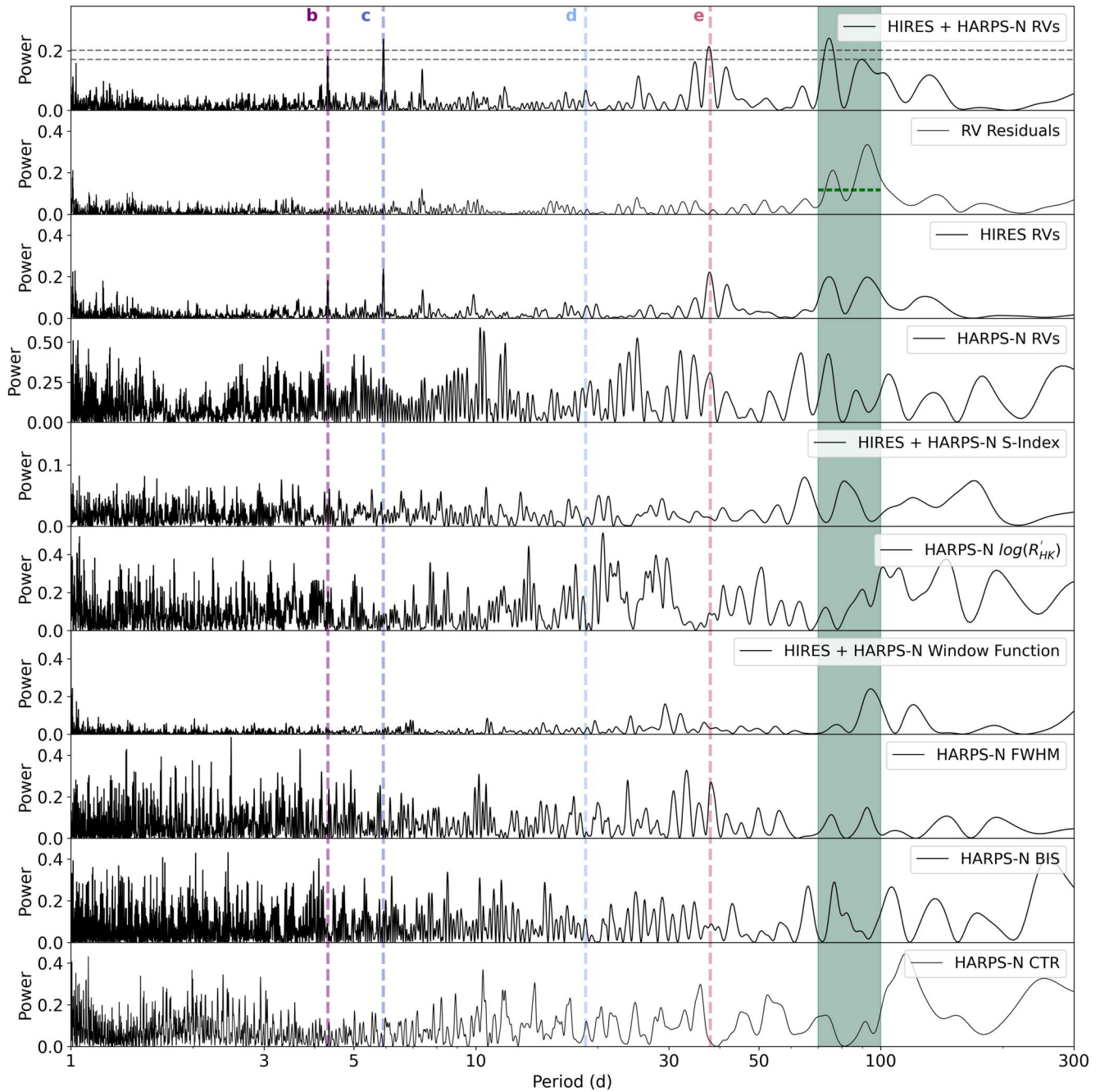


Figure 7. Lomb–Scargle periodograms for the RV data, RV residuals from a four-planet fit, activity indicators, and spectral window function for TOI-1246 using Keck/HIRES and TNG/HARPS-N data (see legends). The vertical colored lines indicate the periods of the four transiting planets in the system (TOI-1246 b: purple, TOI-1246 c: blue, TOI-1246 d: light blue, TOI-1246 e: pink). The green region indicates the range of likely periods for the fifth candidate planet. We consider the peaks at both 76 and 94 d, and choose to report the fifth candidate planet at 94 d in this work. In the top panel, the horizontal dashed lines represent the 1% and 0.1% false-alarm levels. In the second panel, we show two closely spaced horizontal dashed lines in the range of period space we consider. These lines represent the 99.99th percentile of 10,000 bootstrap samples of these residuals, in dark green (for the 76 d signal) and green (for the 94 d signal), and show that both of these signals are statistically significant.

WIYN is less susceptible to the 95 day seasonal window function than Keck (where we collected 100 of 130 RVs), and these RVs will be useful in ascertaining the period, validity, and nature of the long-period signals identified here.

Given that stellar rotation and unmodeled eccentricity are unlikely to be responsible for these long-period signals, and that the signals are robust to bootstrap sampling, we tentatively attribute the signal to a fifth planet candidate with a period of either 76.2 days or 93.8 days. We refer to this planet candidate

as planet f for the remainder of this paper, but emphasize that this does not imply confirmation of this candidate planet.

RV signals from nontransiting planets are expected to be common in systems with transiting planets (He et al. 2021). The correlated RV signals from these unmodeled planets (or other unmodeled signals) can affect the accuracy of mass measurements derived from RV observations (e.g., Cloutier et al. 2017; Bonfils et al. 2018). With this in mind, we inspected the extent to which our choice of underlying planet

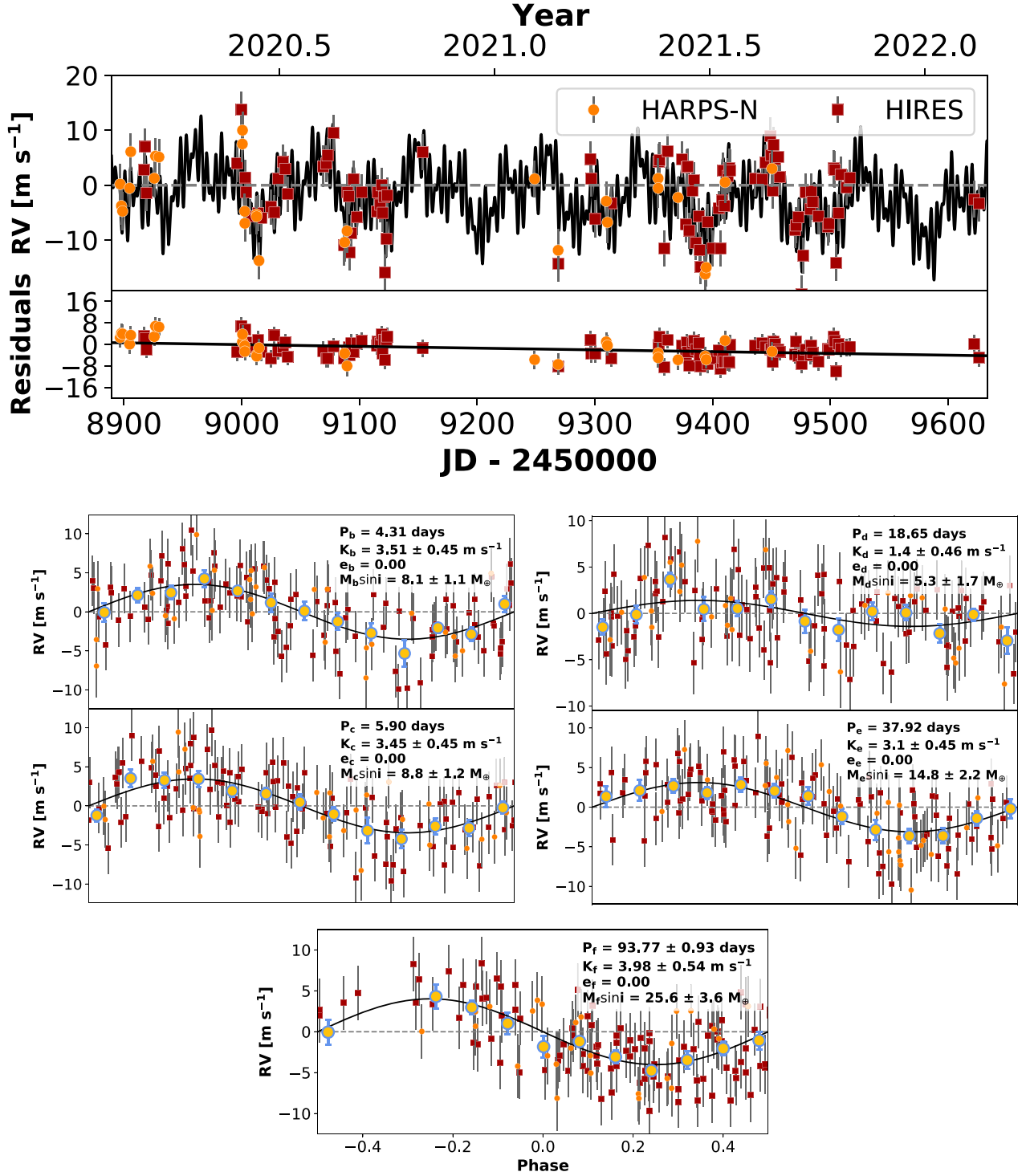


Figure 8. RV data and models for the four transiting planets and a fifth nontransiting planet candidate. The top panel shows the complete RV time series (orange points are TNG/HARPS-N data, and red points are Keck/HIRES) with the preferred five-planet RV model overlaid in black and with residuals (rms = 4.3 m s $^{-1}$) shown below. The five panels beneath this show the RV data phased to each planet's orbital period (with binned data points in yellow and blue), with the other planets' signals removed, and with the RV model overlaid in black.

model affected the masses of the four transiting planets. We considered models with four, five, or six planets (i.e., the four transiting planets with zero, one, or two additional outer planets), and with or without varying eccentricity. We found that the best-fit values for the planets masses were consistent to 1σ . Thus, the uncertainties in the planet masses appear to be dominated by measurement uncertainties, rather than model selection.

We also do not find any unaccounted-for transit events in the TESS photometry (see Section 4.1), implying that this fifth long-period planet candidate is likely nontransiting if it is similar in size to TOI-1246 e. We simulated light curves for TOI-1246 using the continuum flux in the original light curve, and injected planets with a range of radii in order to assess our ability to recover planet transits of various depths. We are able

Table 4

Selected Results of RV Analyses to Compare the Bayesian Inference Criterion (BIC) for Models with Varying Planet Numbers (N_{planets}), and Additional Planet Candidate Period(s)

N_{planets}	Additional Planet Period(s)	Additional Free Parameters	N_{free}	BIC
4	7	741.21
5	76.2 days	$P_f, t_{c,f}, K_f$	10	708.09
5	93.8 days	$P_f, t_{c,f}, K_f$	10	704.53
6	76.0 days and 94.3 days	$P_f, t_{c,f}, P_g, t_{c,g}, K_f, K_g$	13	702.96

Note. All models include the following free parameters: $K_b, K_c, K_d, K_e, \gamma, \dot{\gamma}$. We set the RV jitter terms to constant values determined by an initial five-planet fit in order to reduce the complexity of the model comparison. The five-planet models are preferred relative to the four-planet model.

to identify the individual transits of planets $\gtrsim 4 R_{\oplus}$ by eye, and can recover these signals. Given the minimum mass of $\sim 25 M_{\oplus}$ associated with the fifth planet candidate, Chen & Kipping (2017) predict a radius of $\sim 5 R_{\oplus}$. As a result, we would expect to see evidence of a Neptune-sized long-period fifth planet candidate if it did transit.

4.6. Selecting a Preferred Model

In order to determine which model to select as our preferred fit, we used the Bayesian Inference Criterion (BIC) to compare models (see Table 4). We interpret a $\Delta\text{BIC} > 5$ to indicate a model is preferred. We find that the five-planet models both have lower BICs than the four-planet model by > 5 , and thus are preferred. The five-planet model with $P_f = 93.8$ days has a BIC that is slightly lower than that for the analogous model with $P_f = 76.2$ days, and so we propose a candidate period of 93.8 days. We also considered the BIC for a six-planet model, with two additional planet candidates at 76 d and 94 d. The resulting BIC is smaller than those for the two five-planet models, but since the difference is small and we are hesitant to propose two additional planet candidates in this region of period space, we report the results of the 93.8 d five-planet model.

The minimum mass of the fifth planet candidate resulting from the preferred model is $M \sin i = 25.6 \pm 3.6 M_{\oplus}$, which is much more massive than the four transiting planets and the solar system ice giants. We report the corresponding mass measurements for the transiting planets ($M_b = 8.1 \pm 1.1 M_{\oplus}$, $M_c = 8.8 \pm 1.2 M_{\oplus}$, $M_d = 5.3 \pm 1.7 M_{\oplus}$, and $M_e = 14.8 \pm 2.3 M_{\oplus}$) in Table 3 and show the results of this fit in Figure 8. We discuss the implications of the fifth candidate planet on the system architecture in Section 5.4.

There is still some structure remaining in the RV residuals of the five-planet fit (see the top panel of Figure 8). We performed additional RV fits allowing the eccentricities of one, two, or all of the outer three planets (TOI-1246 d, TOI-1246 e, and the fifth planet candidate) to vary. We find that this does not remove this structure, indicating there is remaining unmodeled signal in the RV data set. We performed bootstrap sampling on these five-planet model residuals, and found that the peak at 76 days is significant in the residuals to $> 99.99\%$. This indicates that the 76 d period signal cannot be explained as an alias of the 93.8 days period. This signal could correspond to a sixth planet candidate with a period of 76 days, but more data are needed in order to investigate this tentative hypothesis.

4.7. Stability

We explored the stability of the system using the SPOCK package (Tamayo et al. 2020). In addition to modeling the system configuration adopted in Section 4.6, we investigated how the stability changed as we varied planet eccentricities and the number of planets within the system. We did not consider the effects of the proper-motion companion TIC 230127303, because of its wide separation with TOI-1246 (~ 750 au).

When considering eccentricity variations, we were inspired by past observational and theoretical work. Ford et al. (2008) predicted the Kepler mission would probe the eccentricity distribution of transiting planets. Several works have investigated subsets of this sample, using transit duration statistics to infer eccentricity distributions (e.g., Fabrycky et al. 2014; Shabram et al. 2016; Xie et al. 2016). Mills et al. (2019) considered a large (~ 1000) sample of planets with high-precision RVs from the California-Kepler Survey, and found that the eccentricity distribution is well-described by a truncated Rayleigh distribution, in agreement with the previous works.

SPOCK estimates the stability of a planetary system with given planet parameters, and generates a probability of orbit stability, i.e., the probability that a planet on a given orbit survives 10^9 orbits. Each simulation is ended and classed as unstable if any planets' Hill spheres overlap (see *Materials and Methods* in Tamayo et al. 2020 for details). Using SPOCK, we evaluated system stability by drawing 10,000 realizations of system parameters from the following distributions:

1. Eccentricity: truncated Rayleigh distribution with a mode of 0.0355 (as per Mills et al. 2019).
2. Orbital Period: held constant at the values reported in Table 3.
3. Stellar Mass: Normal distribution with a mean of $0.87 M_{\odot}$ and a standard deviation of $0.0 M_{\odot}$ (see Table 1).
4. Inclinations: fixed for the four transiting planets with values determined using the impact parameters and semimajor axes reported in Table 3. We used a uniform distribution in the range $[0, 0.1736]$ for $\cos(i)$ for the nontransiting fifth planet candidate. Systems with intrinsically higher multiplicities have lower mutual inclinations (discussed in He et al. 2020), and so a fifth planet candidate will likely be well-aligned with the other planets in this compact multiplanet system.
5. Planet Mass: normal distribution truncated to prevent negative planet masses (this only reduces the parameter space investigated by 0.4% for TOI-1246 d, and not at all for the other planets). The mean and standard deviation for each normal distribution was set by the preferred RV model described in Section 4.6 and reported in Table 3. We used the inclinations described above to calculate planet masses from the minimum masses derived from the RV data.
6. Argument of periastron, ω : uniform distribution in the range $[0, 2\pi]$ for each planet.

We find that 13% of trial systems have > 0.34 probability of persisting over 10^9 orbits, where 0.34 is the cutoff between stability/instability reported in Tamayo et al. (2020). We note that this low stability value is likely due to the destabilizing effect of TOI-1246 e's location near mean-motion resonance with TOI-1246 d. We simulated several system architectures with distributions as described above, except for TOI-1246 e's

Table 5
Results of SPOCK Analysis of System Stability

Number of Planets	Planet Period(s)	Transiting Planets Eccentricity	Fraction of Stable Samples
4		$e_i = 0$	0.15
4		$e_i = \text{TruncatedRayleigh}(\sigma = 0.0355)$	0.13
4		$e_i = 0, e_{.04} = 0.1 \pm 0.1$	0.86
4		$e_i = \text{TruncatedRayleigh}(\sigma = 0.0355), e_{.04} = 0.1 \pm 0.1$	0.11
4	$P_e = 26$ days	$e_i = 0$	0.96
4	$P_e = 45$ days	$e_i = 0$	0.97
5	$P_5 = 76.2$ days	$e_i = \text{TruncatedRayleigh}(\sigma = 0.0355)$	0.08
5	$P_5 = 93.8$ days	$e_i = \text{TruncatedRayleigh}(\sigma = 0.0355)$	0.13
5	$P_5 = 10.5$ days	$e_i = \text{TruncatedRayleigh}(\sigma = 0.0355)$	0.06
5	$P_5 = 26.6$ days	$e_i = \text{TruncatedRayleigh}(\sigma = 0.0355)$	0.03
6	$P_5 = 10.5$ days, $P_6 = 94$ days	$e_i = \text{TruncatedRayleigh}(\sigma = 0.0355)$	0.06
6	$P_5 = 26.6$ days, $P_6 = 94$ days	$e_i = \text{TruncatedRayleigh}(\sigma = 0.0355)$	0.03

Note. For planet periods not specified in the table, we used the reported planet periods from Table 3. For each SPOCK model tested, this table reports the fraction of the 10,000 samples drawn that remain stable, i.e., that have a $\geq 34\%$ probability of persisting over 10^9 orbits.

orbital period, which we varied such that it was no longer near resonance with TOI-1246 d. We find that such systems have substantially higher stability ($>95\%$ of systems have a >0.34 chance of persisting over 10^9 orbits). We will investigate the dynamics of this system more closely in a follow-up work.

We also used SPOCK to simulate only the four transiting planets, in order to consider the scenario where the fifth longer-period RV signal is not planetary in nature. We find that the stability of the four-planet system architecture is similar to that of the scenario including the fifth planet candidate at 93.8 days. Therefore, the presence of a fifth planet candidate does not necessarily destabilize the system.

We also considered how additional undetected planets would affect system stability using SPOCK. The long baseline of both photometric and spectroscopic observations of TOI-1246 mean we are sensitive to detecting planets with a large range of orbital periods. Given that it would be unlikely to miss such a short-period transiting planet with a transit depth similar to that of TOI-1246 b across the long photometric baseline, we are confident that there are no further transiting sub-Neptunes interior to TOI-1246 b. However, the relatively large gaps in period space between TOI-1246c and TOI-1246 d, and between TOI-1246 d and TOI-1246 e raise the question of whether another inner planet could be hiding in the system. We performed two tests to evaluate the likelihood of the system containing another planet interior to TOI-1246 e. In each test, we drew 10,000 samples from the same distributions as described above, and added an additional $1 M_{\oplus}$ planet with a period of 10.5 days or 26.6 days and an inclination of 88° (mean of the inclinations of the other transiting planets). The choice of periods was motivated by Kepler multiplanet statistics. Weiss et al. (2018) show that planets in multiplanet systems are evenly spaced in log-period space, and so we chose to test periods that are evenly spaced in log-period space between the known transiting planets in the TOI-1246 system. Using the mass–radius relation of Wolfgang et al. (2016) for sub-Neptunes, we estimate a corresponding radius of $<1 R_{\oplus}$ (and a corresponding transit depth of <114 ppm). Based on the results of the transit injection and recovery test discussed in Section 4.4, we find that a $1 R_{\oplus}$ test planet could transit but not be detected in transit data. The eccentricity and argument of periastron of the additional planet were drawn from the same distributions as in the default test. We performed these tests both including and excluding the long-period planet candidate

($P = 93.8$ days) found in the RV data. All of these tests resulted in a less stable system (see Table 5), which supports the theory that there are no further planets in the gaps between the detected planets in the system.

5. Results and Discussion

The TOI-1246 system hosts four transiting planets, and we find no evidence of additional transiting planets in the TESS photometry. We measured masses for these four transiting planets, and have found a longer-period signal in the RV data that may be planetary in nature. We also find that the system’s stability is not significantly affected by a fifth planet candidate at 93.8 days. We list the planet properties from this work in Table 3.

Millholland & Winn (2021) find that high-metallicity stars ($[\text{Fe}/\text{H}] > 0.0$) tend to host multiple sub-Neptunes, which are less uniform in size, and TOI-1246 conforms to this statistical prediction. The inner three transiting planets have distinct radii within the sub-Neptune population; TOI-1246c lies at the peak of the radius distribution, while TOI-1246 b resides on the “occurrence cliff” (Fulton et al. 2017). TOI-1246 d and TOI-1246 e are among the largest sub-Neptunes.

5.1. Planet Bulk Densities and Composition

Figure 9 shows the TOI-1246 planets in mass–radius space. We find that the inner three planets in this system have similar masses, while the outermost planet is significantly more massive, with a mass similar to those of the ice giants in our solar system. The fifth planet candidate has a minimum mass of $25.6 \pm 3.6 M_{\oplus}$, which is even greater than the masses of Uranus and Neptune. TOI-1246 b and TOI-1246c have similar masses but distinct radii, and so comparing their atmospheres would be interesting with regard to probing the formation and evolutionary history of the system. The four transiting planets also have quite varied densities: $\rho_b = 1.74 \pm 0.23 \text{ g cm}^{-3}$, $\rho_c = 3.21 \pm 0.44 \text{ g cm}^{-3}$, $\rho_d = 0.70 \pm 0.24 \text{ g cm}^{-3}$, and $\rho_e = 1.62 \pm 0.25 \text{ g cm}^{-3}$. All four transiting planets have densities lower than that of Earth⁵⁹ ($\rho_{\oplus} = 5.514 \text{ g cm}^{-3}$). TOI-1246 b and TOI-1246 e have bulk densities similar to that of Neptune⁶⁰

⁵⁹ <https://nssdc.gsfc.nasa.gov/planetary/factsheet/earthfact.html>

⁶⁰ <https://nssdc.gsfc.nasa.gov/planetary/factsheet/neptunefact.html>

($\rho_{\Psi} = 1.638 \text{ g cm}^{-3}$). Although TOI-1246 d is a sub-Neptune, it has a bulk density similar to that of Saturn⁶¹ ($\rho_{\tau} = 0.67 \text{ g cm}^{-3}$).

The TOI-1246 planets are located in well-populated regions of mass–radius parameter space. TOI-1246 b has a mass of $8.1 \pm 1.1 M_{\oplus}$ and a radius of $2.97 \pm 0.06 R_{\oplus}$. It is consistent in mass and radius with Kepler-28 b (Steffen et al. 2012), Kepler-49 c (Steffen et al. 2013; Rowe et al. 2014; Jontof-Hutter et al. 2016), Kepler-223 b (Rowe et al. 2014; Mills et al. 2016), Kepler-307 b (Xie 2014), and K2-266 d (Rodriguez et al. 2018). These planets are all members of compact multiplanet systems just as TOI-1246 b is. Furthermore, all of these planets exhibit TTVs, and the Kepler-223 system hosts a four-planet near-resonant chain. While TOI-1246 b does not orbit near or in resonance with another planet in the TOI-1246 system, it is interesting to note that all of these planets are in compact multiplanet systems and are either near resonance or have planetary siblings near resonance.

TOI-1246 c ($8.8 \pm 1.2 M_{\oplus}$, $2.47 \pm 0.08 R_{\oplus}$) is consistent in mass and radius with HD 5278 b, K2-138 d (Christiansen et al. 2018), HD 15337c (Gandolfi et al. 2019), and K2-38 c (Sinukoff et al. 2016). HD 5278 b (Sozzetti et al. 2021), which has a insolation flux similar to that of TOI-1246c ($S_c = 129 S_{\oplus}$, $S_{\text{HD 5278 b}} = 132 S_{\oplus}$), highlights how little can be inferred from a planet’s bulk density. All of these planets lie near the 100% H₂O composition line, and yet their masses and radii could be explained by a diversity of compositions. Sozzetti et al. (2021) suggest two options: a “wet” differentiated planet with a substantial water layer and a H/He gas envelope, and a “dry” planet with an iron core and silicate mantle. While Sozzetti et al. (2021) find that sub-Neptunes are expected to retain their volatile contents, the bulk density of TOI-1246c is consistent with a variety of compositions. Atmospheric observations, such as transmission spectroscopy (see Section 5.3), are critical to distinguish between degenerate planet composition models (Rogers & Seager 2010).

TOI-1246 d ($5.3 \pm 1.7 M_{\oplus}$, $3.46 \pm 0.09 R_{\oplus}$) has a mass and a radius that are consistent with those of Kepler-11 d (Lissauer et al. 2011), Kepler-33 e (Lissauer et al. 2012), Kepler-79 e (Rowe et al. 2014), Kepler-177 b (Xie 2014; Jontof-Hutter et al. 2016; Hadden & Lithwick 2017), Kepler-223 c (Rowe et al. 2014) and K2-32 b (Dai et al. 2016). Once again, all of these planets are in multiplanet systems, and all except Kepler-11 d exhibit TTVs, as does TOI-1246 d. Furthermore, the Kepler-79, Kepler-223 and K2-32 systems host multiplanet resonant chains of planets. If the fifth planet candidate in the TOI-1246 system is confirmed to be planetary, and if its period is found to be one of the candidate periods we suggest in this paper, TOI-1246 will also host a resonant chain of planets.

TOI-1246 e ($14.8 \pm 2.3 M_{\oplus}$, $3.72 \pm 0.16 R_{\oplus}$) is consistent in mass and radius with GJ 3470 b, EPIC 249893012c, WASP-47 d, Kepler-1661 b, and Kepler-595 b. Kepler-1661 b is a circumbinary planet that orbits near the hot edge of the habitable zone of a young (1–3 Gyr) binary system (Socia et al. 2020). EPIC 249893012c (Hidalgo et al. 2020), on the other hand, orbits an evolved star with an age of $9.0^{+0.5}_{-0.6}$ Gyr that is just leaving the main sequence. TOI-1246 is intermediate in age, compared to these stars. WASP-47 d (Hellier et al. 2012) and Kepler-595 b (Morton et al. 2016; Yoffe et al. 2021), like TOI-1246 e, are the outer planets in respective pairs near 2:1

resonance. They both show TTVs, as does GJ 3470 b (Bonfils et al. 2012; Awiphan et al. 2016). It is interesting to note that the majority of planets that have masses and radii similar to those of the TOI-1246 planets also show TTVs, and that such planets are almost always found in multiplanet systems.

Having compared the TOI-1246 planets to other planets with precisely known properties, we now consider possible atmospheric compositions for these worlds. The TOI-1246 planets are likely to harbor volatile envelopes that have been sculpted by their proximity to the host star and evolutionary history. We further investigate the potential compositions of these planets using the Exoplanet Composition Interpolator,⁶² which was developed using models from Lopez & Fortney (2014). These models assume an isothermal Earth-like 2:1 rock/iron core, a fully adiabatic interior for the H/He envelope, and a small isothermal radiative atmosphere atop the H/He envelope. This tool uses planet radii, masses, and insolation flux, as well as stellar age, to predict the core mass fraction and envelope mass fraction of each planet. The results of this interpolation indicate that TOI-1246 b has a $\sim 5\%$ H/He envelope, while TOI-1246c has a $\sim 2\%$ H/He envelope, and TOI-1246 d and TOI-1246 e have $\sim 10\%$ H/He envelopes by mass. Due to the uncertainty in the stellar age discussed in Section 3, we evaluated these models for several stellar ages between 5 and 10 Gyr. We find that the results vary by $\sim 1\%$, and the trend of envelope masses across the system does not change, so the envelope fractions reported are robust to larger uncertainties in stellar age than we have reported.

TOI-1246 b lies on the 0.1% H₂ composition curve for a 1000K planet. While TOI-1246 b has an equilibrium temperature of 950K, it is predicted to have a $\sim 5\%$ H/He envelope by mass; thus, it lies far from its predicted location in mass–radius space to the top right of Figure 9. TOI-1246c lies near the 100% H₂O composition curve, and is likely to have a higher-density core (possibly with a substantial water fraction) surrounded by a low-density envelope. TOI-1246 e has a size similar to those of both of the solar system ice giants. Uranus and Neptune have similar internal structures; standard models include a rocky core surrounded by a thick massive icy mantle and a low-mass H/He atmosphere (Podolak et al. 1995). This may indicate a potential composition for TOI-1246 e, but due to inherent degeneracy in mass and radius measurements and the differences in F_{insol} , we cannot conclusively determine the interior structure of TOI-1246 or the other TOI-1246 planets.

5.2. System Architecture

The dynamical architecture of TOI-1246 was previously probed by Dietrich & Apai (2020), who formalized a model (DYNAMITE⁶³) to predict the periods, radii, and inclinations of undetected planets in multiplanet systems using population statistics. They tested the DYNAMITE model on several TESS multiplanet systems, including TOI-1246. At the time of publication, TOI-1246 e was not yet a TOI, and so Dietrich & Apai (2020) considered TOI-1246 as a three-planet system. They predict a fourth planet in the system with a period of $10.4^{+1.93}_{-1.94}$ d, a radius of $2.91^{+0.921}_{-0.737} R_{\oplus}$, and a predicted transit probability of 0.91 ± 0.001 (Table 2 in Dietrich & Apai 2020). If such a planet were transiting, we would expect to detect it in the TESS light curve, as it has a radius and a period similar to

⁶¹ <https://nssdc.gsfc.nasa.gov/planetary/factsheet/saturnfact.html>

⁶² <https://tools.emac.gsfc.nasa.gov/ECI/>

⁶³ <https://github.com/JeremyDietrich/dynamite>

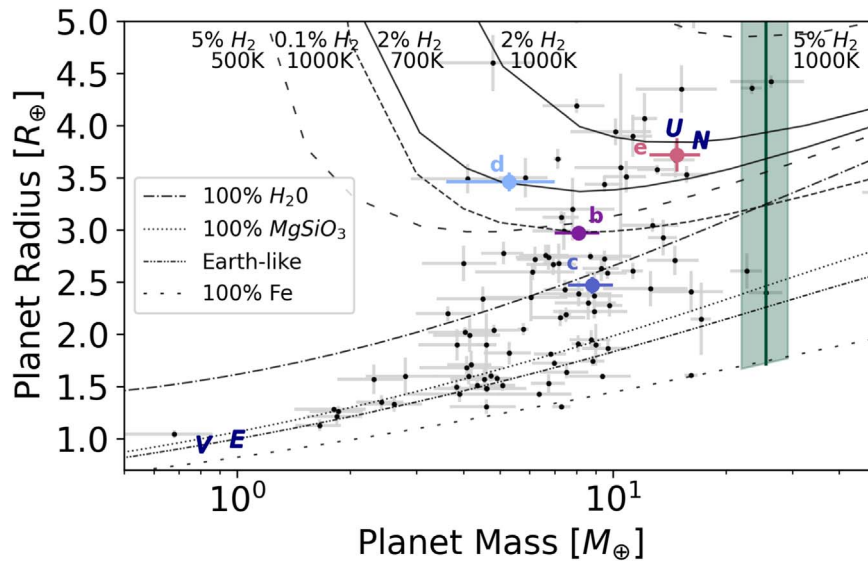


Figure 9. Mass–radius plot showing the four planets orbiting TOI-1246 (TOI-1246 b: purple, TOI-1246 c: blue, TOI-1246 d: light blue, TOI-1246 e: pink). The parameter space that the fifth nontransiting planet candidate could occupy is shown in green (we exclude potential compositions more dense than 100% Fe). Theoretical composition curves from Zeng et al. (2019) are shown in gray. Earth (E), Venus (V), Uranus (U), and Neptune (N) are also shown for context, with the precise masses and radii for these planets lying in the center of the letter symbol. The subset of confirmed planets in systems with two or more planets, and with mass and radius measurements with $>3\sigma$ precision, are plotted in black with gray error bars.

those of other planets in the system. However, we do not find evidence of such a planet in the TESS light curve. Furthermore, extending our SPOCK analysis of system stability to include such a planet destabilizes the system (system stability is reduced by a factor of 2; see Table 5). While the predicted period does not match the actual fourth planet in the system (TOI-1246 e), it does lie evenly between TOI-1246 c and TOI-1246 d in log-period space, as predicted by Kepler multiplanet statistics. Furthermore, the probability distribution in Figure 8 of Dietrich & Apai (2020) does show a smaller peak near the true period of TOI-1246 e. There is some evidence in the RV data of a signal at around 10 d (see Figure 7), but we attribute it to the spectral window function of TNG/HARPS-N observations. Therefore, we find that there is insufficient evidence for a planet at 10 days, although such a low-mass planet in such an orbit is not ruled out by the data. Dietrich & Apai (2020) do not indicate that a fifth planet with a period between 50 and 100 days would be likely, but they only consider the probability normalized to one injected planet, and so this does not preclude a fifth, exterior planet from being a likely addition to the TOI-1246 from a dynamical point of view.

In Figure 10, we compare TOI-1246 to other exoplanetary systems with four confirmed planets with measured radii. We exclude Kepler-37, Kepler-48, Kepler-411, Kepler-65, and WASP-47 because they only have measured radii for three planets. We also exclude HR 8799, for visual clarity, as it hosts four very long-period planets discovered using the direct imaging method. TOI-1246 is one of only five four-planet systems with both measured masses and radii for all planets in the system. The other five systems are KOI-94 (Weiss et al. 2013), K2-32 (Lillo-Box et al. 2020), Kepler-223 (Mills et al. 2016), and Kepler-79 (Jontof-Hutter et al. 2014). Visual inspection of this small sample shows that TOI-1246 has a unique architecture within the group, with two closely packed planets, (at least) two planets farther out, and with the most massive planet farthest from the host star. Furthermore, of this subset of four-planet systems, TOI-1246 is the brightest host star in V magnitude, making it particularly amenable for future

follow-up observations. We note that all four-planet systems with measured masses for any number of planets have bright host stars. This is a consequence of the difficulty of measuring masses in multiplanet systems through the radial velocity method, which is ameliorated somewhat for bright host stars. However, TOI-1246 is brighter than 90% of the 188 systems that host planets exhibiting TTVs,⁶⁴ which have a wide range of V magnitudes (8.93 to 17.02 mag).

5.3. System Formation

Despite the prevalence of sub-Neptune exoplanets (Howard et al. 2012), their formation pathway remains unclear (Bean et al. 2021). Sub-Neptunes are believed to be mostly rocky planets (or water worlds) that, unlike super-Earths, have retained their primary atmospheres (Lopez & Fortney 2014). The most widely discussed formation mechanism is inward movement through the protoplanetary disk (rather than in situ formation; see Inamdar & Schlichting 2015). However, whether this inward movement is through the migration of planetary cores (migration model) or through the drift model, where mass growth mostly takes place close-in, is not known. Regardless of the specific mechanism of inward movement, protoplanets accrete their atmospheres from the gas disk. However, the drift and migration mechanisms do predict different atmospheric compositions: the drift model predicts volatile-poor planets, as pebbles are expected to lose volatiles as they migrate inward across the snow line (Ida et al. 2019), while the migration model predicts a variety of volatile contents across a planetary system (Raymond et al. 2018).

We estimated how much material was available to form the TOI-1246 planets assuming that the TOI-1246 planets formed in situ at their respective semimajor axes in a minimum mass

⁶⁴ NASA Exoplanet Archive (NASA Exoplanet Science Institute 2020), https://exoplanetarchive.ipac.caltech.edu/cgi-bin/TblView/nph-tblView?app=ExoTbls&config=PS&constraint=default_flag=1 accessed 7 November 2021.

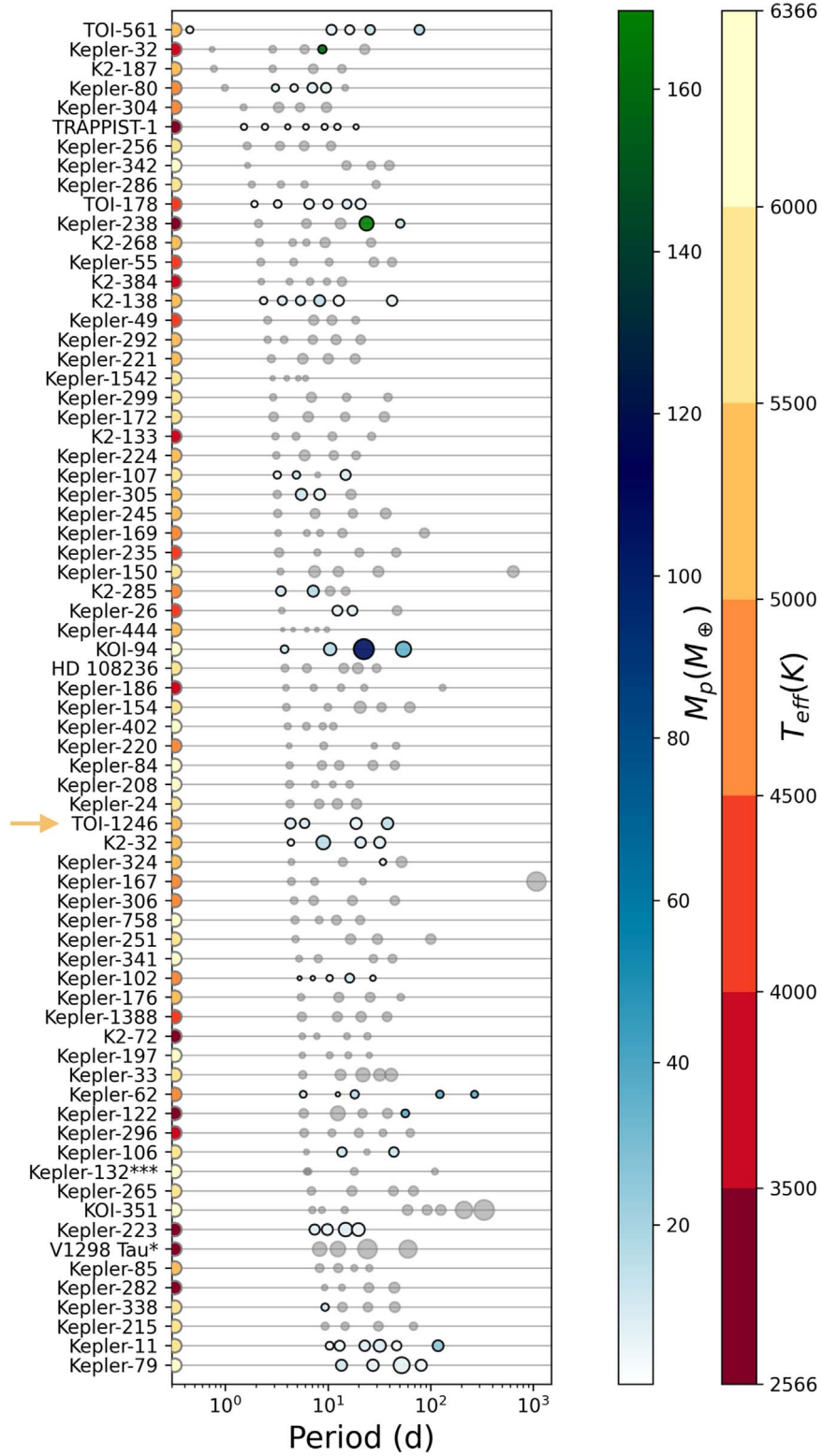


Figure 10. High-multiplicity ($N_p \geq 4$) planet systems where all planets are confirmed and have radius measurements, ordered by increasing innermost orbital period. Point size is determined by planet radius, and planets with measured masses are shaded according to the color bar on the right of the figure. Planets with upper limit mass measurements do not have a black edge, and are colored according to the upper limit. The effective temperatures of the systems' host stars are indicated using the semicircles on the left of each row, shaded according to the second color bar. TOI-1246 is one of only five systems with measured masses for all four planets, and has a unique system architecture within this group. *V1298 Tau and K2-266 are the only systems in this population that are brighter than TOI-1246. **We note that the masses shown for the two outer planets in the Kepler-282 system are nominal TTV masses and are likely overestimates (Xie 2014). ***Kepler-132 is a binary star system that hosts four planets (at 6.2d, 6.4d, 18.0d, and 110d), but it is unknown which planets orbit which star.

solar nebula (MMSN) with a surface density profile for solids

$$\Sigma = 33 F Z_{\text{rel}} \left(\frac{a}{\text{au}} \right)^{-\frac{3}{2}} \text{ g cm}^{-2}. \quad (1)$$

We used $F = 1$ and $Z_{\text{rel}} = 0.33$, as per Chiang & Youdin (2010). We found that, for each planet in the TOI-1246 system, less than 5% of the measured masses would be available at their measured semimajor axes. The total measured masses for all four transiting planets are predicted to be spread across 5.5 au in the disk. We also considered several other surface density prescriptions discussed in Dai et al. (2020), including those described by Chiang & Laughlin (2013) and Schlichting (2014). We find that none of these profiles provide sufficient mass interior to 0.25 au to form the TOI-1246 planets at their measured masses. This indicates that the planets likely migrated inward in the disk to their current observed locations.

Transmission spectroscopy of sub-Neptunes can shed light on the formation mechanism(s) responsible for creating these planets. TOI-1246 is an interesting test bed for investigating sub-Neptune formation, as it hosts four transiting sub-Neptunes (and potentially a fifth nontransiting planet), which share a host star, evolutionary history, and formation environments. We calculated the Transmission and Emission Spectroscopy Metrics (TSM and ESM) as per Kempton et al. (2018), for the four planets in the TOI-1246 system, and report these values in Table 3. These metrics are used to quantify how favorable a planet’s atmosphere may be to transmission and emission spectroscopy. We find that TOI-1246 b and TOI-1246 d are the easiest targets for transmission spectroscopy in the system, with TSMs of 48.9 and 72.7 respectively. Although none of the four planets have $\text{TSM} > 90$, which is recommended for high-quality transmission spectra for 1–4 R_{\oplus} planets, they still present a compelling opportunity to compare the atmospheres of planetary siblings in the same system.

There are eight other multiplanet systems with two or more planets with TSMs equal to or greater than that of TOI-1246 b, which has the second-highest TSM in the TOI-1246 system. Kepler 51 (Steffen et al. 2013; Masuda 2014) is one such system, with two low-density “super-puff” planets that were probed using HST/WFC3 (Libby-Roberts et al. 2020). The planets were found to have featureless spectra, which were interpreted as evidence for high-altitude aerosol layers. Another promising multiplanet system for transmission spectroscopy is TOI-178 (Leleu et al. 2021), which hosts six planets. JWST will observe three of these planets under GO 2319 (PI: Hooton). TOI-1246 presents another opportunity to study the atmospheres of planetary siblings in order to glean information about system formation and evolution, and thus the TOI-1246 planets are compelling targets for the upcoming JWST mission. Furthermore, this transiting multiplanet system could be a benchmark target for the Ariel mission (Edwards et al. 2019), which will study planet formation and evolution as well as TTVs as a complementary science case.

5.4. A Potential Fifth Planet

As discussed in Section 4.4, we find a fifth periodic signal in the RV data at a period exterior to that of TOI-1246 e. We report the results from our preferred model with a fifth nontransiting planet candidate at $P_f = 93.8$ days. Further observations are needed to refine the orbital period and to confirm the nature of this signal, but if it is planetary, it would

be a fifth planet in an already rich multiplanet system. Furthermore, if the period is actually found to be at 76.2 days, this fifth planet will lie very near to the 2:1 resonance with TOI-1246 e, and in turn in 4:1 resonance with TOI-1246 d. This would imply a 4:2:1 resonant chain between these three planets, similar to that between three of Jupiter’s moons: Europa, Ganymede, and Io. Such a result will allow us to probe deeper into the formation history of this system. It is thought that few resonant chains remain stable after the gas disk dissipates (Ogihara & Ida 2009), although Terquem & Papaloizou (2007) posit that planet pairs near commensurability (rather than in strict commensurability) may survive this era of destabilization.

The presence of an additional planet candidate in the system may also explain the need for more RV observations than predicted in order to fully model the known planet candidates (He et al. 2021). This motivates us to continue collecting RV data for this system, to determine the period and characterize the nature of this planet candidate while also improving the accuracy of the mass measurements for the four known transiting planets.

6. Conclusion

The main conclusions of this work are as follows:

1. We confirm four transiting sub-Neptunes around K dwarf TOI-1246, and measure the masses of TOI-1246 b and TOI-1246 c to $>7\sigma$ precision, of TOI-1246 e to $>6\sigma$ precision, and of TOI-1246 d to 3σ precision.
2. We report the following masses for the four transiting planets: $M_b = 8.1 \pm 1.1 M_{\oplus}$, $M_c = 8.8 \pm 1.2 M_{\oplus}$, $M_d = 5.3 \pm 1.7 M_{\oplus}$, and $M_e = 14.8 \pm 2.3 M_{\oplus}$. We note that these measurements are robust to variations in the assumed planet eccentricities ($e_i < 1$) and number of planets ($4 \leq N_p \leq 6$).
3. We fit the TESS photometry in order to refine planet radii estimates, and we report the following radii: $R_b = 2.97 \pm 0.06 R_{\oplus}$, $R_c = 2.47 \pm 0.08 R_{\oplus}$, $R_d = 3.46 \pm 0.09 R_{\oplus}$, and $R_e = 3.72 \pm 0.16 R_{\oplus}$. We also find no evidence of additional transiting planets in the TESS time series data.
4. The four transiting planets have relatively low bulk densities ($0.70 - 3.21 \text{ g cm}^{-3}$), indicating that these planets have volatile H/He envelopes, and we predict that the four planets have quite varied envelope mass fractions.
5. We find a fifth periodic signal in the RV data, which may correspond to a planet on an orbit exterior to that of TOI-1246 e. We suggest a candidate orbital period (93.8 days), and emphasize the need for additional RV observations to determine the period and characterize the nature of this signal. We include this fifth planet candidate in our RV fits and report a minimum mass of $M \sin(i) = 25.6 \pm 3.6 M_{\oplus}$ (which is also a 7σ mass measurement), but we note that the mass depends on the true orbital period.
6. We find that TOI-1246 d and TOI-1246 e exhibit TTVs, due to their nearness to the 2:1 mean-motion resonance.
7. We use the SPOCK framework (Tamayo et al. 2020) to investigate the stability of this system, and find that additional undetected planets between the known transiting planets would destabilize the system. Adding the fifth planet candidate exterior to TOI-1246 e does not decrease the system stability.

8. We consider the system architecture of the TOI-1246 system in the context of other high-multiplicity systems, and find that few systems have similar patterns in period spacing.

TOI-1246 is a rich multiplanet system that hosts at least four sub-Neptune planets with a diversity of masses and potential compositions. Additional data will allow us to more fully characterize the fifth nontransiting planet candidate, continue to investigate TTVs, and characterize the atmospheres of these planetary siblings in the context of their host star.

We thank the time assignment committees of the University of California, the California Institute of Technology, NASA, and the University of Hawaii for supporting the TESS-Keck Survey with observing time at Keck Observatory. We thank NASA for funding associated with our Key Strategic Mission Support project. We gratefully acknowledge the efforts and dedication of the Keck Observatory staff for support of HIRES and remote observing. We recognize and acknowledge the very significant cultural role and reverence that the summit of Maunakea has within the indigenous Hawaiian community. We are deeply grateful to have the opportunity to conduct observations from this mountain. We thank Ken and Gloria Levy, who supported the construction of the Levy Spectrometer on the Automated Planet Finder. We thank the University of California and Google for supporting Lick Observatory, and the UCO staff for their dedicated work scheduling and operating the telescopes of Lick Observatory. This paper is based on data collected by the TESS mission. Funding for the TESS mission is provided by the NASA Explorer Program.

This paper includes data collected by the TESS mission. Funding for the TESS mission is provided by NASA's Science Mission Directorate. We acknowledge the use of public TOI Release data from pipelines at the TESS Science Office and at the TESS Science Processing Operations Center. Resources supporting this work were provided by the NASA High-End Computing (HEC) Program through the NASA Advanced Supercomputing (NAS) Division at Ames Research Center for the production of the SPOC data products. This research has made use of the Exoplanet Follow-up Observation Program website, which is operated by the California Institute of Technology, under contract with the National Aeronautics and Space Administration under the Exoplanet Exploration Program. This research has also made use of the NASA Exoplanet Archive, which is operated by the California Institute of Technology, under contract with the National Aeronautics and Space Administration under the Exoplanet Exploration Program.

This work also makes use of observations from the LCOGT network. Part of the LCOGT telescope time was granted by NOIRLab through the Mid-Scale Innovations Program (MSIP). MSIP is funded by NSF.

This work has made use of data from the European Space Agency (ESA) mission Gaia (<https://www.cosmos.esa.int/gaia>), processed by the Gaia Data Processing and Analysis Consortium (DPAC; <https://www.cosmos.esa.int/web/gaia/dpac/consortium>). Funding for the DPAC has been provided by national institutions, in particular the institutions participating in the Gaia Multilateral Agreement.

This research was made possible through the use of the AAVSO Photometric All-Sky Survey (APASS), funded by the

Robert Martin Ayers Sciences Fund and NSF AST-1412587. This publication also makes use of data products from the Two Micron All Sky Survey, which is a joint project of the University of Massachusetts and the Infrared Processing and Analysis Center/California Institute of Technology, funded by the National Aeronautics and Space Administration and the National Science Foundation.

This publication makes use of data products from the Wide-field Infrared Survey Explorer, which is a joint project of the University of California, Los Angeles, and the Jet Propulsion Laboratory/California Institute of Technology, funded by the National Aeronautics and Space Administration.

This work is based on observations made with the Italian Telescopio Nazionale Galileo (TNG) operated on the island of La Palma by the Fundación Galileo Galilei of the INAF (Istituto Nazionale di Astrofisica) at the Spanish Observatorio del Roque de los Muchachos of the Instituto de Astrofísica de Canarias under programs CAT19A_162, ITP19_1 and A41TAC_49. Part of this work is done under the framework of the KESPRINT collaboration (<http://kesprint.science>). KESPRINT is an international consortium devoted to the characterization and research of exoplanets discovered with space-based missions. This work is partly financed by the Spanish Ministry of Economics and Competitiveness through grants PGC2018-098153-B-C31.

Some of the observations in the paper made use of the High-Resolution Imaging instrument Alopeke obtained under Gemini LLP Proposal Number: GN/S-2021A-LP-105. Alopeke was funded by the NASA Exoplanet Exploration Program and built at the NASA Ames Research Center by Steve B. Howell, Nic Scott, Elliott P. Horch, and Emmett Quigley. Alopeke was mounted on the Gemini North telescope of the international Gemini Observatory, a program of NSF's NOIR Lab, which is managed by the Association of Universities for Research in Astronomy (AURA) under a cooperative agreement with the National Science Foundation on behalf of the Gemini partnership: the National Science Foundation (United States), National Research Council (Canada), Agencia Nacional de Investigación y Desarrollo (Chile), Ministerio de Ciencia, Tecnología e Innovación (Argentina), Ministério da Ciência, Tecnologia, Inovações e Comunicações (Brazil), and Korea Astronomy and Space Science Institute (Republic of Korea).

C.D. gratefully acknowledges support from the David & Lucile Packard Foundation and the Alfred P. Sloan Foundation. A.A.B., B.S.S., and I.A.S. acknowledge the support of the Ministry of Science and Higher Education of the Russian Federation under the grant 075-15-2020-780(N13.1902.21.0039). J.K. gratefully acknowledges the support of the Swedish National Space Agency (SNSA; DNR 2020-00104). A.W.M. is supported by the NSF Graduate Research Fellowship grant No. DGE 1752814. J.M.A. M. is supported by the National Science Foundation Graduate Research Fellowship Program under grant No. DGE-1842400. J. M.A.M. acknowledges the LSSTC Data Science Fellowship Program, which is funded by LSSTC, NSF Cybertraining grant No. 1829740, the Brinson Foundation, and the Moore Foundation; his participation in the program has benefited this work. C.K. H. acknowledges support from the National Science Foundation Graduate Research Fellowship Program under grant No. DGE 2146752. M.R. is supported by the National Science Foundation Graduate Research Fellowship Program under grant No. DGE-1752134. R.A.R. is supported by an NSF Graduate Research

Fellowship, grant No. DGE 1745301. P.D. is supported by a National Science Foundation (NSF) Astronomy and Astrophysics Postdoctoral Fellowship under award AST-1903811. R.L. acknowledges financial support from the Centre of Excellence “Severo Ochoa” award to the Instituto de Astrofísica de Andalucía (SEV-2017-0709). D.H. acknowledges support from the Alfred P. Sloan Foundation and the National Aeronautics and Space Administration (80NSSC20K0593, 80NSSC21K0652). T.M. acknowledges financial support from the Spanish Ministry of Science and Innovation (MICINN) through the Spanish State Research Agency, under the Severo Ochoa Program 2020-2023 (CEX2019-000920-S). K.W.F.L. acknowledges support by DFG grants RA714/14-1 within the DFG Schwerpunkt SPP 1992, “Exploring the Diversity of Extrasolar Planets.”

This research made use of Lightcurve, a Python package for Kepler and TESS data analysis (Lightcurve Collaboration, 2018). This research also made use of Astropy,⁶⁵ a community-developed core Python package for Astronomy (Astropy Collaboration et al. 2013, 2018). This research made use of *exoplanet* and its dependencies (Astropy Collaboration et al. 2013; Kipping 2013; Salvatier et al. 2016; Theano Development Team 2016; Astropy Collaboration et al. 2018; Luger et al. 2019; Van Eylen et al. 2019; Agol et al. 2020; Foreman-Mackey et al. 2020). This work made use of *tpfplotter* by J. Lillo-Box (publicly available at www.github.com/jlillo/tpfplotter), which also made use of the python packages Astropy, Lightcurve, Matplotlib, and NumPy.

Facilities: TESS, Keck:I (HIRES), TNG (HARPS-N), Keck: II (NIRC2), Gemini:Gillett (‘Alopec’, LCOGT, Dragonfly Telephoto Array, TRES (Tillinghast), CAHA (Astralux), Exoplanet Archive, Gaia.

Software: Astropy (Astropy Collaboration et al. 2013, 2018), Astroquery (Ginsburg et al. 2019), batman (Kreidberg 2015), emcee (Foreman-Mackey et al. 2013), SpecMatch (Petigura et al. 2017), *exoplanet* (Agol et al. 2020), Lightcurve (Lightcurve Collaboration et al. 2018), RadVel (Fulton et al. 2018), SPOCK (Tamayo et al. 2020), Transit Least Squares (Hippke & Heller 2019), *kiauhoku* (Claytor et al. 2020), Matplotlib (Hunter 2007), NumPy (Harris et al. 2020), *astrasens* (Lillo-Box et al. 2012, 2014), AstroImageJ (Collins et al. 2017), TAPIR (Jensen 2013), *celerite* (Foreman-Mackey et al. 2017).

ORCID iDs

Emma V. Turtelboom  <https://orcid.org/0000-0002-1845-2617>

Lauren M. Weiss  <https://orcid.org/0000-0002-3725-3058>

Courtney D. Dressing  <https://orcid.org/0000-0001-8189-0233>

Grzegorz Nowak  <https://orcid.org/0000-0002-7031-7754>

Enric Pallé  <https://orcid.org/0000-0003-0987-1593>

Corey Beard  <https://orcid.org/0000-0001-7708-2364>

Sarah Blunt  <https://orcid.org/0000-0002-3199-2888>

Casey Brinkman  <https://orcid.org/0000-0002-4480-310X>

Ashley Chontos  <https://orcid.org/0000-0003-1125-2564>

Zachary R. Claytor  <https://orcid.org/0000-0002-9879-3904>

Fei Dai  <https://orcid.org/0000-0002-8958-0683>

Paul A. Dalba  <https://orcid.org/0000-0002-4297-5506>

Steven Giacalone  <https://orcid.org/0000-0002-8965-3969>

Caleb K. Harada  <https://orcid.org/0000-0001-5737-1687>

Michelle L. Hill  <https://orcid.org/0000-0002-0139-4756>


Rae Holcomb  <https://orcid.org/0000-0002-5034-9476>

Judith Korth  <https://orcid.org/0000-0002-0076-6239>

Jack Lubin  <https://orcid.org/0000-0001-8342-7736>

Thomas Masseron  <https://orcid.org/0000-0002-6939-0831>

Mason MacDougall  <https://orcid.org/0000-0003-2562-9043>

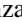
Andrew W. Mayo  <https://orcid.org/0000-0002-7216-2135>

Teo Močnik  <https://orcid.org/0000-0003-4603-556X>

Joseph M. Akana Murphy  <https://orcid.org/0000-0001-8898-8284>

Alex S. Polanski  <https://orcid.org/0000-0001-7047-8681>


Malena Rice  <https://orcid.org/0000-0002-7670-670X>


Ryan A. Rubenzahl  <https://orcid.org/0000-0003-3856-3143>

Nicholas Scarsdale  <https://orcid.org/0000-0003-3623-7280>

Keivan G. Stassun  <https://orcid.org/0000-0002-3481-9052>


Dakotah B. Tyler  <https://orcid.org/0000-0003-0298-4667>

Judah Van Zandt  <https://orcid.org/0000-0002-4290-6826>

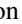
Hans J. Deeg  <https://orcid.org/0000-0003-0047-4241>

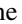
Benjamin Fulton  <https://orcid.org/0000-0003-3504-5316>


Davide Gandolfi  <https://orcid.org/0000-0001-8627-9628>


Andrew W. Howard  <https://orcid.org/0000-0001-8638-0320>

Dan Huber  <https://orcid.org/0000-0001-8832-4488>

Howard Isaacson  <https://orcid.org/0000-0002-0531-1073>

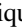
Stephen R. Kane  <https://orcid.org/0000-0002-7084-0529>

Kristine W. F. Lam  <https://orcid.org/0000-0002-9910-6088>

Rafael Luque  <https://orcid.org/0000-0002-4671-2957>

Eduardo L. Martín  <https://orcid.org/0000-0002-1208-4833>

Giuseppe Morello  <https://orcid.org/0000-0002-4262-5661>

Jaume Orell-Miquel  <https://orcid.org/0000-0003-2066-8959>

Erik A. Petigura  <https://orcid.org/0000-0003-0967-2893>

Paul Robertson  <https://orcid.org/0000-0003-0149-9678>

Arpita Roy  <https://orcid.org/0000-0001-8127-5775>

Vincent Van Eylen  <https://orcid.org/0000-0001-5542-8870>

David Baker  <https://orcid.org/0000-0002-2970-0532>

Alexander A. Belinski  <https://orcid.org/0000-0003-3469-0989>

Allyson Bieryla  <https://orcid.org/0000-0001-6637-5401>

David R. Ciardi  <https://orcid.org/0000-0002-5741-3047>

Karen A. Collins  <https://orcid.org/0000-0001-6588-9574>

Devin J. Della-Rose  <https://orcid.org/0000-0002-6042-7351>

E. Furlan  <https://orcid.org/0000-0001-9800-6248>

Tianjun Gan  <https://orcid.org/0000-0002-4503-9705>

Crystal L. Gnlika  <https://orcid.org/0000-0003-2519-6161>


Pere Guerra  <https://orcid.org/0000-0002-4308-2339>

Steve B. Howell  <https://orcid.org/0000-0002-2532-2853>

Mary Jimenez  <https://orcid.org/0000-0002-5000-9316>

David W. Latham  <https://orcid.org/0000-0001-9911-7388>

Kathryn V. Lester  <https://orcid.org/0000-0002-9903-9911>

Jorge Lillo-Box  <https://orcid.org/0000-0003-3742-1987>

Christopher R. Mann  <https://orcid.org/0000-0002-9312-0073>

Peter P. Plavchan  <https://orcid.org/0000-0002-8864-1667>


Boris Safonov  <https://orcid.org/0000-0003-1713-3208>

Ivan A. Strakhov  <https://orcid.org/0000-0003-0647-6133>

Justin M. Wittrock  <https://orcid.org/0000-0002-7424-9891>

Douglas A. Caldwell  <https://orcid.org/0000-0003-1963-9616>

Zahra Essack  <https://orcid.org/0000-0002-2482-0180>

Jon M. Jenkins  <https://orcid.org/0000-0002-4715-9460>

⁶⁵ <http://www.astropy.org>

Elisa V. Quintana  <https://orcid.org/0000-0003-1309-2904>
 George R. Ricker  <https://orcid.org/0000-0003-2058-6662>
 Roland Vanderspek  <https://orcid.org/0000-0001-6763-6562>
 S. Seager  <https://orcid.org/0000-0002-6892-6948>
 Joshua N. Winn  <https://orcid.org/0000-0002-4265-047X>

References

- Agol, E., & Fabrycky, D. C. 2018, in *Handbook of Exoplanets*, ed. H. J. Deeg & J. A. Belmonte (Cham: Springer), 7
- Agol, E., Luger, R., & Foreman-Mackey, D. 2020, *AJ*, **159**, 123
- Astropy Collaboration, Robitaille, T. P., Tollerud, E. J., et al. 2013, *A&A*, **558**, A33
- Astropy Collaboration, Price-Whelan, A. M., Sipőcz, B. M., et al. 2018, *AJ*, **156**, 123
- Avallone, E. A., Tayar, J., van Saders, J. L., Berger, T. A., & Claytor, Z. R. 2021, *BAAS*, **53**, 2021n6i314p07
- Awiphan, S., Kerins, E., Pichadee, S., et al. 2016, *MNRAS*, **463**, 2574
- Ballard, S., Fabrycky, D., Fressin, F., et al. 2011, *ApJ*, **743**, 200
- Baranne, A., Queloz, D., Mayor, M., et al. 1996, *A&AS*, **119**, 373
- Bean, J. L., Raymond, S. N., & Owen, J. E. 2021, *JGRE*, **126**, e06639
- Bonfanti, A., Delrez, L., Hooton, M. J., et al. 2021, *A&A*, **646**, A157
- Bonfils, X., Gillon, M., Udry, S., et al. 2012, *A&A*, **546**, A27
- Bonfils, X., Almenara, J. M., Cloutier, R., et al. 2018, *A&A*, **618**, A142
- Brown, T. M., Baliber, N., Bianco, F. B., et al. 2013, *PASP*, **125**, 1031
- Buchhave, L. A., Bakos, G. Á., Hartman, J. D., et al. 2010, *ApJ*, **720**, 1118
- Buchhave, L. A., Latham, D. W., Johansen, A., et al. 2012, *Natur*, **486**, 375
- Butler, R. P., Marcy, G. W., Fischer, D. A., et al. 1999, *ApJ*, **526**, 916
- Butler, R. P., Marcy, G. W., Williams, E., et al. 1996, *PASP*, **108**, 500
- Canto Martins, B. L., Gomes, R. L., Messias, Y. S., et al. 2020, *ApJS*, **250**, 20
- Chen, J., & Kipping, D. 2017, *ApJ*, **834**, 17
- Chiang, E., & Laughlin, G. 2013, *MNRAS*, **431**, 3444
- Chiang, E., & Youdin, A. N. 2010, *AREPS*, **38**, 493
- Chontos, A., Akana Murphy, J. M., MacDougall, M. G., et al. 2021, arXiv:2106.06156
- Christiansen, J. L., Crossfield, I. J. M., Barentsen, G., et al. 2018, *AJ*, **155**, 57
- Ciardi, D. R., Beichman, C. A., Horch, E. P., & Howell, S. B. 2015, *ApJ*, **805**, 16
- Claret, A. 2017, *A&A*, **600**, A30
- Claytor, Z. R., van Saders, J. L., Llama, J., et al. 2022, *ApJ*, **927**, 219
- Claytor, Z. R., van Saders, J. L., Santos, Á. R. G., et al. 2020, *kiauhoku: Stellar model grid interpolation*, Astrophysics Source Code Library, ascl:2011.027
- Cloutier, R., Astudillo-Defru, N., Doyon, R., et al. 2017, *A&A*, **608**, A35
- Coelho, P., Barbuy, B., Meléndez, J., Schiavon, R. P., & Castilho, B. V. 2005, *A&A*, **443**, 735
- Collins, K. 2019, *AAS Meeting Abstracts*, **233**, 140.05
- Collins, K. A., Kielkopf, J. F., Stassun, K. G., & Hessman, F. V. 2017, *AJ*, **153**, 77
- Dai, F., Winn, J. N., Albrecht, S., et al. 2016, *ApJ*, **823**, 115
- Dai, F., Roy, A., Fulton, B., et al. 2020, *AJ*, **160**, 193
- Danieli, S., Lokhorst, D., Zhang, J., et al. 2020, *ApJ*, **894**, 119
- Dawson, R. I., & Fabrycky, D. C. 2010, *ApJ*, **722**, 937
- Demangeon, O. D. S., Zapatero Osorio, M. R., Alibert, Y., et al. 2021, *A&A*, **653**, A41
- Dietrich, J., & Apai, D. 2020, *AJ*, **160**, 107
- Edwards, B., Mugnai, L., Tinetti, G., Pascale, E., & Sarkar, S. 2019, *AJ*, **157**, 242
- Efron, B. 1979, *AnSta*, **7**, 1, <https://www.jstor.org/stable/2958830>
- ExoFOP 2019, Exoplanet Follow-up Observing Program—TESS, IPAC, doi:10.26134/EXOFOF3
- Fabrycky, D. C., Lissauer, J. J., Ragozzine, D., et al. 2014, *ApJ*, **790**, 146
- Fűrész, G. 2008, PhD thesis, University of Szeged
- Findeisen, K., Hillenbrand, L., & Soderblom, D. 2011, *AJ*, **142**, 23
- Fischer, D. A., Marcy, G. W., Butler, R. P., Laughlin, G., & Vogt, S. S. 2002, *ApJ*, **564**, 1028
- Ford, E. B., Quinn, S. N., & Veras, D. 2008, *ApJ*, **678**, 1407
- Foreman-Mackey, D., Agol, E., Ambikasaran, S., & Angus, R. 2017, *AJ*, **154**, 220
- Foreman-Mackey, D., Hogg, D. W., Lang, D., & Goodman, J. 2013, *PASP*, **125**, 306
- Foreman-Mackey, D., Luger, R., Czekala, I., et al. 2020, *exoplanet-dev/exoplanet v0.3.2*, Zenodo, doi:10.5281/zenodo.1998447
- Fulton, B. J., Petigura, E. A., Blunt, S., & Sinukoff, E. 2018, *PASP*, **130**, 044504
- Fulton, B. J., Petigura, E. A., Howard, A. W., et al. 2017, *AJ*, **154**, 109
- Furlan, E., Ciardi, D. R., Everett, M. E., et al. 2017, *AJ*, **153**, 71
- Gaia Collaboration 2018, *yCat*, **1**/345
- Gandolfi, D., Fossati, L., Livingston, J. H., et al. 2019, *ApJL*, **876**, L24
- Ginsburg, A., Sipőcz, B. M., Brasseur, C. E., et al. 2019, *AJ*, **157**, 98
- Guerrero, N. M., Seager, S., Huang, C. X., et al. 2021, *ApJS*, **254**, 39
- Hadden, S., Barclay, T., Payne, M. J., & Holman, M. J. 2019, *AJ*, **158**, 146
- Hadden, S., & Lithwick, Y. 2017, *AJ*, **154**, 5
- Hara, N. C., Boué, G., Laskar, J., & Correia, A. C. M. 2017, *MNRAS*, **464**, 1220
- Harris, C. R., Millman, K. J., van der Walt, S. J., et al. 2020, *Natur*, **585**, 357
- He, M. Y., Ford, E. B., & Ragozzine, D. 2021, *AJ*, **162**, 216
- He, M. Y., Ford, E. B., Ragozzine, D., & Carrera, D. 2020, *AJ*, **160**, 276
- Hellier, C., Anderson, D. R., Collier Cameron, A., et al. 2012, *MNRAS*, **426**, 739
- Hidalgo, D., Pallé, E., Alonso, R., et al. 2020, *A&A*, **636**, A89
- Hipke, M., & Heller, R. 2019, *A&A*, **623**, A39
- Høg, E., Fabricius, C., Makarov, V. V., et al. 2000, *A&A*, **355**, L27
- Hormuth, F., Brandner, W., Hippler, S., & Henning, T. 2008, *JPhCS*, **131**, 012051
- Howard, A. W., Johnson, J. A., Marcy, G. W., et al. 2010, *ApJ*, **721**, 1467
- Howard, A. W., Marcy, G. W., Bryson, S. T., et al. 2012, *ApJS*, **201**, 15
- Howell, S. B., Everett, M. E., Horch, E. P., et al. 2016, *ApJL*, **829**, L2
- Howell, S. B., Everett, M. E., Sherry, W., Horch, E., & Ciardi, D. R. 2011, *AJ*, **142**, 19
- Huang, C. X., Shporer, A., Dragomir, D., et al. 2018, arXiv:1807.11129
- Hunter, J. D. 2007, *CSE*, **9**, 90
- Ida, S., Yamamura, T., & Okuzumi, S. 2019, *A&A*, **624**, A28
- Inamdar, N. K., & Schlichting, H. E. 2015, *MNRAS*, **448**, 1751
- Isaacson, H., & Fischer, D. 2010, *ApJ*, **725**, 875
- Jenkins, J. M., Twicken, J. D., McCauliff, S., et al. 2016, *Proc. SPIE*, **9913**, 99133E
- Jensen, E. 2013, *Tapir: A web interface for transit/eclipse observability*, Astrophysics Source Code Library, ascl:1306.007
- Jontof-Hutter, D., Lissauer, J. J., Rowe, J. F., & Fabrycky, D. C. 2014, *ApJ*, **785**, 15
- Jontof-Hutter, D., Ford, E. B., Rowe, J. F., et al. 2016, *ApJ*, **820**, 39
- Kempton, E. M. R., Bean, J. L., Louie, D. R., et al. 2018, *PASP*, **130**, 114401
- Kipping, D. M. 2013, *MNRAS*, **435**, 2152
- Kreidberg, L. 2015, *PASP*, **127**, 1161
- Kurucz, R. L. 1992, in *IAU Symp. 149, The Stellar Populations of Galaxies*, ed. B. Barbuy & A. Renzini (Dordrecht: Kluwer), 225
- Kurucz, R. L. 1993, *yCat*, **VI**/39
- Lacedelli, G., Malavolta, L., Borsato, L., et al. 2021, *MNRAS*, **501**, 4148
- Lam, K. W. F., Korth, J., Masuda, K., et al. 2020, *AJ*, **159**, 120
- Leleu, A., Alibert, Y., Hara, N. C., et al. 2021, *A&A*, **649**, A26
- Lester, K. V., Matson, R. A., Howell, S. B., et al. 2021, *AJ*, **162**, 75
- Libby-Roberts, J. E., Berta-Thompson, Z. K., Désert, J.-M., et al. 2020, *AJ*, **159**, 57
- Lightkurve Collaboration, Cardoso, J. V. D. M., Hedges, C., et al. 2018, *Lightkurve: Kepler and TESS time series analysis in Python*, Astrophysics Source Code Library, ascl:1812.013
- Lillo-Box, J., Barrado, D., & Bouy, H. 2012, *A&A*, **546**, A10
- Lillo-Box, J., Barrado, D., & Bouy, H. 2014, *A&A*, **566**, A103
- Lillo-Box, J., Lopez, T. A., Santerne, A., et al. 2020, *A&A*, **640**, A48
- Lissauer, J. J., Fabrycky, D. C., Ford, E. B., et al. 2011, *Natur*, **470**, 53
- Lissauer, J. J., Marcy, G. W., Rowe, J. F., et al. 2012, *ApJ*, **750**, 112
- Lithwick, Y., Xie, J., & Wu, Y. 2012, *ApJ*, **761**, 122
- Lomb, N. R. 1976, *Ap&SS*, **39**, 447
- Lopez, E. D., & Fortney, J. J. 2014, *ApJ*, **792**, 1
- Luger, R., Agol, E., Foreman-Mackey, D., et al. 2019, *AJ*, **157**, 64
- Mamajek, E. E., & Hillenbrand, L. A. 2008, *ApJ*, **687**, 1264
- Mandel, K., & Agol, E. 2002, *ApJL*, **580**, L171
- Masuda, K. 2014, *ApJ*, **783**, 53
- Mathur, S., García, R. A., Régulo, C., et al. 2010, *A&A*, **511**, A46
- McCurly, C., Volgenau, N. H., Harbeck, D.-R., et al. 2018, *Proc. SPIE*, **10707**, 107070K
- McQuillan, A., Aigrain, S., & Mazeh, T. 2013, *MNRAS*, **432**, 1203
- Millholland, S. C., & Winn, J. N. 2021, *ApJL*, **920**, L34
- Mills, S. M., Fabrycky, D. C., Migaszewski, C., et al. 2016, *Natur*, **533**, 509
- Mills, S. M., Howard, A. W., Petigura, E. A., et al. 2019, *AJ*, **157**, 198
- Morton, T. D., Bryson, S. T., Coughlin, J. L., et al. 2016, *ApJ*, **822**, 86
- NASA Exoplanet Science Institute 2020, *Planetary Systems Table*, IPAC
- Ogihara, M., & Ida, S. 2009, *ApJ*, **699**, 824
- Parviainen, H. 2015, *MNRAS*, **450**, 3233
- Parviainen, H., & Korth, J. 2020, *MNRAS*, **499**, 3356
- Petigura, E. A., Howard, A. W., Marcy, G. W., et al. 2017, *AJ*, **154**, 107

- Podolak, M., Weizman, A., & Marley, M. 1995, *P&SS*, **43**, 1517
- Raymond, S. N., Boulet, T., Izidoro, A., Esteves, L., & Bitsch, B. 2018, *MNRAS*, **479**, L81
- Rodriguez, J. E., Becker, J. C., Eastman, J. D., et al. 2018, *AJ*, **156**, 245
- Rogers, L. A., & Seager, S. 2010, *ApJ*, **712**, 974
- Rowe, J. F., Bryson, S. T., Marcy, G. W., et al. 2014, *ApJ*, **784**, 45
- Salvatier, J., Wiecki, T. V., & Fonnesbeck, C. 2016, *PeerJ Comp. Sci.*, **2**, e55
- Savitzky, A., & Golay, M. J. E. 1964, *Anal. Chem.*, **36**, 1627
- Scargle, J. D. 1982, *ApJ*, **263**, 835
- Schlegel, D. J., Finkbeiner, D. P., & Davis, M. 1998, *ApJ*, **500**, 525
- Schlichting, H. E. 2014, *ApJL*, **795**, L15
- Scott, N. J., Howell, S. B., Gnilka, C. L., et al. 2021, *FrASS*, **8**, 138
- Shabram, M., Demory, B.-O., Cisewski, J., Ford, E. B., & Rogers, L. 2016, *ApJ*, **820**, 93
- Sinukoff, E., Howard, A. W., Petigura, E. A., et al. 2016, *ApJ*, **827**, 78
- Smith, J. C., Stumpe, M. C., Van Cleve, J. E., et al. 2012, *PASP*, **124**, 1000
- Socia, Q. J., Welsh, W. F., Orosz, J. A., et al. 2020, *AJ*, **159**, 94
- Sozzetti, A., Damasso, M., Bonomo, A. S., et al. 2021, *A&A*, **648**, A75
- Stassun, K. G., Collins, K. A., & Gaudi, B. S. 2017, *AJ*, **153**, 136
- Stassun, K. G., Corsaro, E., Pepper, J. A., & Gaudi, B. S. 2018a, *AJ*, **155**, 22
- Stassun, K. G., & Torres, G. 2016, *AJ*, **152**, 180
- Stassun, K. G., & Torres, G. 2021, *ApJL*, **907**, L33
- Stassun, K. G., Oelkers, R. J., Pepper, J., et al. 2018b, *AJ*, **156**, 102
- Steffen, J. H., Fabrycky, D. C., Ford, E. B., et al. 2012, *MNRAS*, **421**, 2342
- Steffen, J. H., Fabrycky, D. C., Agol, E., et al. 2013, *MNRAS*, **428**, 1077
- Strehl, K. 1902, *AN*, **158**, 89
- Stumpe, M. C., Smith, J. C., Catanzarite, J. H., et al. 2014, *PASP*, **126**, 100
- Stumpe, M. C., Smith, J. C., Van Cleve, J. E., et al. 2012, *PASP*, **124**, 985
- Tamayo, D., Cranmer, M., Hadden, S., et al. 2020, *PNAS*, **117**, 18194
- Terquem, C., & Papaloizou, J. C. B. 2007, *ApJ*, **654**, 1110
- Theano Development Team 2016, arXiv:1605.02688
- Torrence, C., & Compo, G. P. 1998, *BAMS*, **79**, 61
- Torres, G., Andersen, J., & Giménez, A. 2010, *A&ARv*, **18**, 67
- Van Eylen, V., & Albrecht, S. 2015, *ApJ*, **808**, 126
- Van Eylen, V., Albrecht, S., Huang, X., et al. 2019, *AJ*, **157**, 61
- van Saders, J. L., Ceillier, T., Metcalfe, T. S., et al. 2016, *Natur*, **529**, 181
- van Saders, J. L., & Pinsonneault, M. H. 2013, *ApJ*, **776**, 67
- Vogt, S. S., Allen, S. L., Bigelow, B. C., et al. 1994, *Proc. SPIE*, **2198**, 362
- Weiss, L. M., Marcy, G. W., Rowe, J. F., et al. 2013, *ApJ*, **768**, 14
- Weiss, L. M., Marcy, G. W., Petigura, E. A., et al. 2018, *AJ*, **155**, 48
- Weiss, L. M., Dai, F., Huber, D., et al. 2021, *AJ*, **161**, 56
- Wilson, O. C. 1978, *ApJ*, **226**, 379
- Wizinowich, P., Acton, D. S., Shelton, C., et al. 2000, *PASP*, **112**, 315
- Wolfgang, A., Rogers, L. A., & Ford, E. B. 2016, *ApJ*, **825**, 19
- Wolszczan, A., & Frail, D. A. 1992, *Natur*, **355**, 145
- Wright, J. T., & Howard, A. W. 2009, *ApJS*, **182**, 205
- Xie, J.-W. 2014, *ApJS*, **210**, 25
- Xie, J.-W., Dong, S., Zhu, Z., et al. 2016, *PNAS*, **113**, 11431
- Yee, S. W., Tamayo, D., Hadden, S., & Winn, J. N. 2021, *AJ*, **162**, 55
- Yoffe, G., Ofir, A., & Aharonson, O. 2021, *ApJ*, **908**, 114
- Zechmeister, M., Reiners, A., Amado, P. J., et al. 2018, *A&A*, **609**, A12
- Zeng, L., Jacobsen, S. B., Sasselov, D. D., et al. 2019, *PNAS*, **116**, 9723